Combined carbon, hydrogen, and clumped isotope fractionations reveal differential reversibility of hydrogenotrophic methanogenesis in laboratory cultures

Jeemin H. Rhim[a,1,*] and Shuhei Ono[a]

[a] *Department of Earth, Atmospheric and Planetary Sciences, Massachusetts Institute of Technology, Cambridge, MA 02139, USA. jrhim@alum.mit.edu (J. H. Rhim), sono@mit.edu (S. Ono)*
[1] *Present address: Department of Earth Sciences, Dartmouth College, Hanover, NH 03755, USA*
[*] *Corresponding author: jrhim@alum.mit.edu*

Abstract

Stable isotope analysis has been widely used to aid the source identification of methane. However, the isotopic ($^{13}C/^{12}C$ and D/H) and isotopologue ($^{13}CH_3D$ and $^{12}CH_2D_2$) signatures of microbial methane in natural environments are often different from those in laboratory cultures in which methanogens are typically grown under optimal conditions. Growth phase and hydrogen (H_2) concentration have been proposed as factors controlling the isotopic compositions of methane, but their effects on the relationship among carbon, hydrogen and doubly-substituted "clumped" isotopologue systems have not been assessed in a quantitative framework. Here we experimentally investigate the bulk ($\delta^{13}C$ and δD) and clumped ($\Delta^{13}CH_3D$) isotopologue compositions of methane produced by hyperthermophilic hydrogenotrophic (CO_2-reducing) methanogens using batch and fed-batch systems at different growth phases and H_2 mixing ratios (*Methanocaldococcus bathoardescens* at 82 or 60 °C and on 80 or 25% H_2; *Methanothermobacter thermautotrophicus* ΔH at 65 °C and on 20, 5 or 1.6% H_2). We observed a large range (18 to 63‰) of carbon isotope fractionations, with larger values observed during later growth phase, consistent with previous observations. In contrast, hydrogen isotope fractionations remained relatively constant at –317 ± 25‰. Linear growth was observed for experiments with *M. bathoardescens*, suggesting that dissolution of gaseous H_2 into liquid media became the rate limit as cell density increased. Accordingly, the low (and undersaturated) dissolved H_2 concentrations can explain the increased carbon isotope fractionations during the later growth phase. The δD and $\Delta^{13}CH_3D$ values indicated departure from equilibrium throughout experiments. As the cell density increased and dissolved H_2 decreased, $\Delta^{13}CH_3D$ decreased (further departure from equilibrium), contrary to expectations from previous models. Our isotopologue flow network model reproduced the observed trends when the last H-addition step is less reversible relative to the first three H-addition steps (up to CH_3-CoM). In this differential reversibility model, carbon, hydrogen and clumped isotopologue fractionations are largely controlled by the reversibility of the first three H-addition steps under high H_2 concentrations; the last H-addition step becomes important under low H_2. The magnitude of depletion and decreasing trend in $\Delta^{13}CH_3D$ values were reproduced when a large (≥6‰) secondary clumped kinetic isotope effect was considered in the model. This study highlights the advantage of combined bulk and clumped isotope analyses and the importance of physiological factors (growth phase) and energy availability (dissolved H_2 concentration) when using isotope analyses to aid the source identification of methane.

1 Introduction

Methane (CH$_4$) is an important energy source, a potent greenhouse gas as well as a potential biosignature in subsurface and extraterrestrial environments. Stable carbon (δ^{13}C) and hydrogen (δD) isotope ratios have been extensively used to apportion the relative contributions of different methanogenic pathways, e.g., acetoclastic *vs*. hydrogenotrophic methanogenesis (Welhan and Lupton, 1987; Whiticar, 1990; Sherwood Lollar et al., 2002; Flores et al., 2008; Sherwood Lollar et al., 2008; Pohlman et al., 2009; Baldassare et al., 2014). More recently, technological advances have allowed the precise measurements of the abundance of multiply-substituted or "clumped" isotopologues of methane (e.g., ^{13}CH$_3$D and ^{12}CH$_2$D$_2$; Ono et al., 2014; Stolper et al., 2014; Young et al., 2016; Gonzalez et al., 2019). Methane clumped isotopologue abundance has in some cases served as an isotopic geothermometer and provided temperature estimates that are consistent with environmental temperatures (e.g., Stolper et al., 2015; Wang et al., 2015; Young et al., 2017).

While both bulk and clumped isotopic compositions of methane can help identify the source(s) of methane, some factors complicate the interpretation of the isotopic signatures. For example, overlapping isotopic signatures in δ^{13}C and δD often lead to ambiguous source identifications (e.g., Schoell, 1988; Whiticar, 1990, 1999; Pohlman et al., 2009; Etiope and Sherwood Lollar, 2013), and some microbial methane samples from surface environments have yielded unreasonably high temperature estimates for clumped isotopologue equilibrium (e.g., Stolper et al., 2015; Wang et al., 2015; Douglas et al., 2017; Young et al., 2017). In particular, there are significant discrepancies between the bulk and clumped isotopic signatures observed in natural samples of microbial methane and those produced by laboratory cultures that presumably use the same metabolic pathway (Stolper et al., 2015; Wang et al., 2015; Okumura et al., 2016; Young et al., 2017; Gruen et al., 2018). In general, the δ^{13}C and δD values of microbial methane

2

66   in marine environments, where hydrogenotrophic methanogenesis is thought to be a primary

67   methanogenic pathway, tend to indicate isotopic equilibrium with CO_2 and H_2O. In contrast, the

68    $\delta^{13}C$ and δD values observed in laboratory cultures often indicate kinetic isotope effect (i.e.,

69   departure from equilibrium). Similarly, the $\Delta^{13}CH_3D$ values, representing the relative abundance

70   of $^{13}CH_3D$ clumped isotopologues, measured from microbial methane in marine and deep

71   subsurface sediments indicate internal isotopic equilibrium whereas those from pure cultures carry

72   strong kinetic isotope signatures (Stolper et al., 2015; Wang et al., 2015; Douglas et al., 2017;

73   Young et al., 2017; Gruen et al., 2018).

74   Previous studies that investigated the factors controlling isotope fractionation during

75   microbial methanogenesis shed some light on the cause of the observed discrepancy. Multiple

76   studies have investigated the changes in the carbon isotope fractionation factor ($^{13}\alpha$) during

77   hydrogenotrophic methanogenesis and have identified growth phase and/or hydrogen partial

78   pressure (pH_2) as important controlling factors (Games and Hayes, 1978; Fuchs et al., 1979a;

79   Belyaev et al., 1983; Balabane et al., 1987; Krzycki et al., 1987; Botz et al., 1996; Valentine et al.,

80   2004; Penning et al., 2005; Londry et al., 2008; Yoshioka et al., 2008; Hattori et al., 2012;

81   Okumura et al., 2016; Topçuoğlu et al., 2019; Nguyen et al., 2020). In general, carbon isotope

82   fractionation increases at low pH_2 such that the apparent magnitude of fractionation is close to that

83   expected at CH_4-CO_2 equilibrium. These observations corroborate the differential reversibility

84   hypothesis, which predicts that the variation in carbon isotope fractionation is a result of the

85   changes in reversibility in the enzymatic steps of the hydrogenotrophic methanogenesis pathway

86   (Valentine et al., 2004).

87   The effect of pH_2 on hydrogen isotope fractionation has been investigated by comparing

88   pure cultures grown on high concentrations of H_2 against cocultures containing hydrogenotrophic

3

89   methanogens and syntrophic heterotrophic bacteria (e.g., *Syntropothermus lipocalidus* str. TGB-

90   C1 and *Methenothermobacter thermautotrophicus* str. ΔH) (Yoshioka et al., 2008; Hattori et al.,

91   2012; Okumura et al., 2016). Cocultures provide a means to create relatively low H_2 conditions

92   (e.g., 6.8 to 64.9 Pa; Okumura et al., 2016) compared to high pH_2 conditions ($>10^5$ Pa) often used

93   for pure cultures grown on H_2. So far, to the best of our knowledge, no experiment has observed

94   the magnitude of hydrogen isotope fractionation expected at CH_4-H_2O equilibrium (*ca*. –178‰ at

95   25 °C; Horita and Wesolowski, 1994; Gropp, Iron and Halevy, 2021) that is often observed in

96   natural samples of microbial methane. If the differential reversibility hypothesis can be applied to

97   hydrogen isotope system, higher reversibility and near-equilibrium hydrogen isotope fractionation

98   are expected at lower H_2 environments. This would suggest that the H_2 concentrations tested in

99   experiments so far were not low enough to produce near-equilibrium hydrogen isotope signatures.

100   Laboratory experiments with methane clumped isotope data have only been conducted in

101   batch cultures under high pH_2 conditions (e.g., Stolper et al., 2015; Wang et al., 2015; Young et

102   al., 2017; Gruen et al., 2018). Isotope models relating the dissolved H_2 concentration and $\Delta^{13}CH_3D$

103   values have been proposed and predict changes in $\Delta^{13}CH_3D$ values toward equilibrium (i.e.,

104   increase in $\Delta^{13}CH_3D$ values toward 6‰ at 25 °C) at low H_2 concentrations (e.g., Stolper et al.,

105   2015; Wang et al., 2015), consistent with the overall concept of the differential reversibility

106   hypothesis. However, direct investigations of $\Delta^{13}CH_3D$ values produced at different growth phases

107   or H_2 concentrations are needed to validate whether the differential reversibility model can be

108   applied to clumped isotopologue systematics.

109   In this study, we cultured two different species of methanogens, *Methanocaldococcus*

110   *bathoardescens* and *Methanothermobacter thermautotrophicus* str. ΔH, in batch and fed-batch

111   systems under a pH_2 range from 1.6 kPa to 80 kPa and simultaneously measured $\delta^{13}C$ and δD of

112   the substrates (CO_2 and H_2O) as well as the $\delta^{13}C$, δD and $\Delta^{13}CH_3D$ of the product (CH_4). We

113   present isotopologue flow network model results along with the estimated dissolved H_2

114   concentrations and measured isotopologue ratios to explain the observed fractionation trends by

115   the effects of differential reversibility at the last H-addition step. We propose the $\delta^{13}C$, δD and

116      $\Delta^{13}CH_3D$ trajectories expected for a wide range of dissolved H_2 concentrations encompassing both

117   natural environments and experimental conditions (10^{-9} to 10^{-2} M H_2) that can be applied for future

118   investigations of these isotope signatures for source identifications of methane.

2   Materials and Methods

119

2.1   Organisms

120

121   Cultures of *Methanocaldococcus bathoardescens* were provided by James F. Holden (University

122   of Massachusetts, Amherst). Culture medium for *M. bathoardescens* was prepared following the

123   "282 mod" recipe (Ver Eecke *et al.*, 2012) containing (L^{-1}): 0.34 g KCl, 4.00 g $MgCl_2 \cdot 6H_2O$, 0.14

124   g KH_2PO_4, 3.45 g $MgSO_4 \cdot 7H_2O$, 18 g NaCl, 0.25 g NH_4Cl, 0.14 g $CaCl_2 \cdot 2H_2O$, 2.0 mL

125      $Fe(NH_4)_2(SO_4)_2 \cdot 6H_2O$ (0.1% w/v), 10.0 mL trace element solution SL-10 (DSMZ 320), 5.00 g

126      $NaHCO_3$, 10.0 mL vitamins solution (DSMZ 141). Resazurin was omitted, and 2 mM cysteine and

127   1 mM sulfide were used as reducing agents instead of dithiothreitol.

128   *Methanothermobacter thermautotrophicus* str ΔH (DSM 1053) was purchased from the

129   German Collection of Microorganisms and Cell Cultures (DSMZ, Braunschweig, Germany). The

130   seed culture was transferred to and maintained in mineral medium modified from DSMZ 1523

131   containing (L^{-1}): 0.50 g KH_2PO_4, 0.40 g $MgSO_4 \cdot 7H_2O$, 0.40 g NaCl, 0.40 g NH_4Cl, 0.05 g

132      $CaCl_2 \cdot 2H_2O$, 1.00 mL trace element solution SL-10 (DSMZ 320), 4.00 g $NaHCO_3$, 1.00 mL

133   vitamins solution (DSMZ 503). The medium was reduced with 1 mM sulfide.

2.2 Culture conditions

Table 1 summarizes the conditions for culture experiments conducted in this study. *M. bathoardescens* was grown at 82 or 60 °C and on 80 or 25% H_2, and *M. thermautotrophicus* ΔH was grown at 65 °C and on 20, 5 or 1.6% H_2.

2.2.1 Batch cultures

M. bathoardescens batch culture series was prepared in 100 mL of "282mod" medium described above in 200 mL bottles with 2 bars absolute pressure of H_2/CO_2 (80:20). Each bottle was inoculated with 2% (v/v) of pre-culture in exponential growth phase. Cultures were incubated at 82 °C. At given timepoints, culture headspace was sampled for gas chromatography and $\delta^{13}C_{CO2}$ analysis. Medium was sampled for cell counts with a counting chamber (CTL-HEMM-GLDR, LW Scientific; depth = 0.1 mm) and phase-contrast light microscope. Immediately after sampling, the entire remaining culture was sacrificed by adding 5 mL of 1 M sodium hydroxide. The headspace of a killed culture was used for methane purification and subsequent isotopologue analysis.

2.2.2 Fed-batch cultures

All fed-batch culturing experiments were carried out using a 2-L glass bioreactor (Ace Glass) equipped with a fritted gas dispersion tube (Ace Glass), pH meter (ML-05990-40; Cole-Parmer), temperature monitor/controller, liquid sampling port and a condenser leading to the gas outlet (Figure 1). Both the culturing apparatus and 1.7 L of medium were sterilized by autoclaving at 121 °C for 20 minutes. A set of mass flow controllers was used to control the flow rates of H_2, CO_2 and He (or N_2) to achieve desired mixing ratios of H_2, xH_2, (80, 25, 20, 5 and 1.6%) in the influent gas (Table 1). A column filled with copper was placed between the gas tanks and the

156   reactor and heated to 450 °C to remove trace amounts of oxygen in the incoming gas mixture

157   (Wolfe, 2011). After the reactor was heated to desired temperatures (82, 65 or 60 °C), vitamin

158   solution was added and the pH was adjusted to 6.0 and 7.0 (for *M. bathoardescens* and *M.*

159   *thermautotrophicus*, respectively) while bubbling with the gas mixture (20% CO_2). Cysteine (2

160   mM) and sulfide (2 mM) or cysteine (2 mM) and titanium citrate (0.1 mM) were added as reducing

161   agents before adding a 2% (v/v) of inoculum. Effluent gas from the reactor was passed through a

162   condenser (12 °C) which is followed by an additional column filled with $CaCl_2$ for water removal,

163   and directly connected to an on-line gas chromatography system or a gas sampling bag (Cali-5-

164   Bond™, Calibrated Instruments, Inc., McHenry, MD, USA) (Figure 1).

165   2.3   Analytical procedures

166   2.3.1   Gas chromatography

167   Mixing ratios of headspace gases were measured using a gas chromatograph (GC-2014, Shimadzu,

168   Columbia, MD, USA), equipped with a packed column (Carboxen-1000, 5' by 1/8", Supelco,

169   Bellefonte, PA, USA) with argon carrier gas at 140 °C. A thermal conductivity and a methanizer-

170   flame ionization detector were used to quantify the mixing ratios of H_2, N_2, CH_4 and CO_2. The

171   following compositions of commercial and in-house standard gases were used for calibration: 7%

172   CO, 15% CO_2, 4% O_2, 4.5% CH_4 balanced in N_2 (Supelco; P/N 501743); 4% CH_4, 20% CO_2, 2%

173   CO balanced in N_2 (MESA International Technologies, Inc.); 80% H_2, 20% CO_2 (Airgas). The

174   accuracy of GC analyses was ±5% of measured values. Headspace samples from experiments B.82

175   and F.82.80 were analyzed via manual syringe injection, and all other experiments were measured

176   on-line GC using a gas sampling valve with a 500μL injection loop (VC-SL500CW, VICI Valco,

177   Houston, TX, USA) (Figure 1).

178   2.3.2 $\delta^{13}C_{CO2}$ analysis

179   The carbon isotopic composition of headspace CO_2 ($\delta^{13}C_{CO2}$) was measured using an isotope-ratio

180   mass spectrometer (IRMS; MAT 253, Thermo-Fisher). CO_2 from subsamples of the headspace gas

181   collected from serum bottles (batch cultures) or at the exhaust (fed-batch cultures) was purified by

182   cryogenically separating water and CO_2 from H_2, N_2 and CH_4 into a cold trap at -196 °C and

183   warming up the trap to -80 °C and freezing the eluted CO_2 in a sample vial. Typical analytical

184   precision for $\delta^{13}C$ analysis is ± 0.2‰.

185   2.3.3 δD_{H2O} analysis

186   The hydrogen isotopic composition of media water (δD_{H2O}) was measured using cavity ring-down

187   spectrometry (L-1102i WS-CRDS, Picarro, Sunnyvale, CA, USA) at the University of

188   Massachusetts Amherst. Samples were vaporized at 110 °C. International reference standards

189   (IAEA, Vienna, Austria) were used to calibrate the instrument to the VSMOW-VSLAP scale and

190   working standards were used with each analytical run. Long-term averages of internal laboratory

191   standard analytical results yield an instrumental precision of 0.5‰.

192   2.3.4   Methane isotopologue analysis

193   Methane samples were purified following the preparative GC method described by Wang et al.

194   (2015). For batch culture experiment (B.82), the entire headspace of each killed serum bottle was

195   replaced with helium during the sample preparation. For fed-batch experiments, multi-layer foil

196   sampling bags (Cali-5-Bond™, Calibrated Instruments, Inc., McHenry, MD, USA) used to collect

197   downstream headspace gas at the exhaust were directly connected to the sample preparation system.

198   The relative abundances of methane isotopologues $^{12}CH_4$, $^{13}CH_4$, $^{12}CH_3D$ and $^{13}CH_3D$ were

8

199   measured using a tunable infrared laser direct absorption spectroscopy (TILDAS) described

200   previously (Ono et al., 2014; Wang et al., 2015).

201   2.3.5   Isotope notation and calculation of isotope fractionation factors

202   Bulk isotope values are reported using standard delta notation:

$$\delta^{13}C = \frac{(^{13}C/^{12}C)_{sample}}{(^{13}C/^{12}C)_{VPDB}} - 1 \qquad \text{(Eqn. 1)}$$

$$\delta D = \frac{(D/H)_{sample}}{(D/H)_{VSMOW}} - 1 \qquad \text{(Eqn. 2)}$$

203   where VPDB and VSMOW are Vienna Pee Dee Belemnite and Vienna Standard Mean Ocean

204   Water, respectively. The factor of 1000 was omitted from (Eqn. 1) and (Eqn. 2), following the

205   IUPAC recommendations (Coplen, 2011). Natural gas samples with published $\delta^{13}C$ and δD values

206   (NGS-1 and NGS-3) were used for the calibration of $\delta^{13}C$ and δD values of methane analyzed via

207   TILDAS (Wang et al., 2015). Experimental samples were considered to contain methane

208   isotopologues at or sufficiently close to their natural abundances, hence the following

209   approximations are valid within analytical uncertainty: $^{13}C/^{12}C \approx [^{13}CH_4]/[^{12}CH_4]$ and $D/H \approx \frac{1}{4}$

210    $[^{12}CH_3D]/[^{12}CH_4]$. The abundance of $^{13}CH_3D$ clumped isotopologue is reported as $\Delta^{13}CH_3D$, a

211   metric representing the deviation of the abundance of $^{13}CH_3D$ from a random distribution of

212   isotopes among isotopologues $^{12}CH_4$, $^{13}CH_4$, $^{12}CH_3D$ and $^{13}CH_3D$ (Ono et al., 2014; Wang et al.,

213   2015):

$$\Delta^{13}CH_3D = \frac{[^{13}CH_3D][^{12}CH_4]}{[^{13}CH_4][^{12}CH_3D]} - 1 \qquad \text{(Eqn. 3)}$$

214 The value of $\Delta^{13}CH_3D$ was calibrated by equilibrating methane at 250 °C using Pt catalyst (Ono

215 et al., 2014).

216 The isotope fractionation factor (α) is defined as the ratio of relative abundances of isotopes

217 between a substrate and its product. For a batch experiment (B.82), isotope fractionation factors

218 are calculated assuming an irreversible closed system isotope effect, based on the conventional

219 Rayleigh equation (Mariotti et al., 1981). For the reduction of CO_2 to CH_4:

$$(^{13}\alpha - 1) \cdot \ln f = \ln \frac{\delta^{13}C + 1}{\delta^{13}C_0 + 1} \qquad \text{(Eqn. 4)}$$

220 where f is the fraction of CO_2 remaining; $^{13}\alpha$ is the kinetic isotope fractionation factor for $^{13}C/^{12}C$;

221 and $\delta^{13}C_0$ is the initial isotopic compositions of CO_2.

222 The bulk isotope fractionation factors for fed-batch experiments (F.82.80, F.60.80, F.82.25,

223 F.65.20 and F.65.5) were calculated as follows:

$$^{13}\alpha_{CH4/CO2} = \frac{\delta^{13}C_{CH4} + 1}{\delta^{13}C_{CO2} + 1} \qquad \text{(Eqn. 5)}$$

$$^{2}\alpha_{CH4/H2O} = \frac{\delta D_{CH4} + 1}{\delta D_{H2O} + 1} \qquad \text{(Eqn. 6)}$$

224 The equilibrium fractionation factors for carbon ($^{13}\alpha_{eq}$; Horita, 2001), hydrogen ($^{2}\alpha_{eq}$; Horibe and

225 Craig, 1995) and clumped ($\Delta^{13}CH_3D_{eq}$; Ono et al., 2014) isotope systems were calculated based

226 on experimental and/or theoretical calibrations.

227 2.3.6 Data processing

228 Methanogenesis reaction,

$$CO_{2(g)} + 4\ H_{2(g)} \rightarrow CH_{4(g)} + 2\ H_2O_{(l)} \qquad \text{(Eqn. 7)}$$

229   consumes 5 molecules of gas and produce 1 molecule of gas and water that is mostly in liquid

230   phase. Because of this decrease in volume, the flow rate of effluent gas (Q_{out}) does not equal to the

231   flow rate of the influent gas (Q_{in}: 200 mL/min) and can be lower by up to 25% for our experimental

232   conditions. Based on the stoichiometry of the reaction (Eqn. 7), the flow rate of effluent gas was

233   calculated from the mixing ratios of H_2 and CH_4:

$$Q_{out} = \frac{x_{H2}^{in}}{4x_{CH4}^{out} + x_{H2}^{out}} \cdot Q_{in} \qquad \text{(Eqn. 8)}$$

234   where x_{H2}^{in} and x_{H2}^{out} are H_2 mixing ratios of the influent and effluent gases, respectively, and x_{CH4}^{out}

235   is CH_4 mixing ratio of the effluent gas measured by the GC.

236   The total methane production rate (MPR; mol/hr) was calculated from GC measurements

237   of x_{CH4}^{out} and Q_{out} calculated above:

$$MPR = \frac{P}{RT} \cdot Q_{\text{out}} \cdot x_{CH4}^{out} \qquad \text{(Eqn. 9)}$$

238   where R is gas constant (8.314 $m^3 \cdot Pa/mol/K$), and T and P are temperature (K) and headspace

239   pressure ($\approx 10^5$ Pa) during measurements. Cell-specific MPR (csMPR; mol/cell/hr) was calculated

240   by dividing MPR by the total number of cells in the reactor:

$$csMPR = \frac{MPR}{N_c \cdot V_{\text{liq}}} \qquad \text{(Eqn. 10)}$$

241   where N_c is cell density (cells/m^3), V_{liq} is the volume of media (m^3).

242   2.3.7   Estimating dissolved H_2 concentrations in the liquid medium

243   For our experiments, the concentration of dissolved H_2, [H_2], is lower than what is expected from

244   the saturation gas solubility and pH_2 in the influent gas. This is because of 1) high water vapor

245   pressure in the reactor headspace during hyperthermophilic experiments and 2) the slow kinetics

246   of H_2 dissolution from gas phase to liquid media. We considered the following to estimate $[H_2]$.

247   Water vapor pressure at saturation (pH_2O_{sat}) can be as high as 0.51 bars at 82 °C, 0.25 bars

248   at 65 °C, and 0.20 bars at 60 °C (Haynes et al., 2016). If headspace gas was saturated with water

249   vapor, pH_2 in the gas headspace for our fed-batch reactor can be lower by a factor of two compared

250   to dry gas mixing ratios measured by GC. To consider the water vapor pressure in headspace (and

251   bubbles), we estimated the pH_2O-corrected $pH_{2,VP}$ as:

$$pH_{2,VP} = xH_2 \cdot (p_{reactor} - pH_2O_{sat}) \qquad \text{(Eqn. 11)}$$

252   where $p_{reactor}$ is the total pressure of reactor, pH_2O_{sat} is the saturation water vapor pressure

253   calculated as a function of temperature. The total pressure of reactor was assumed to be 1 bar.

254   Headspace pressures were measured without inoculation and did not exceed over 1.05 bars.

255   In addition, the mass transport limit of H_2 from gas to dissolved phases can result in

256   significant discrepancies between actual $[H_2]$ and the $[H_2]$ values expected at saturation with the

257   gas phase H_2 (e.g., Pauss et al., 1990; Jud et al., 1997). The mass balance of H_2 for the liquid phase

258   can be expressed as:

$$\frac{d[H_2]}{dt} = -(H_2 \text{ consumption rate}) + k_L a \cdot \left(K_H pH_{2,VP} - [H_2]\right) \qquad \text{(Eqn. 12)}$$

259   where H_2 consumption rate is 4 times the *MPR*, and $k_L a$ is the global mass transfer coefficient (e.g.,

260   hr^{-1}), which quantifies the rate of mass transfer for the whole reactor under a specific experimental

261   condition. K_H is the Henry's law constant for H_2 (mol/L/Pa), calculated as a function of

262   temperature and salinity following Chabab et al. (2020). The steady state solution for (Eqn. 12) is:

263

$$[H_2] = K_H \cdot pH_{2,VP} - \frac{4 \cdot MPR}{k_L a}$$

(Eqn. 13)

264   The values of $k_L a$ were estimated based on the following equation:

$$k_L a = \frac{D}{\delta \cdot V_{\text{liq}}} \cdot a$$

(Eqn. 14)

265   where D is the diffusivity coefficient for H_2 (m^2/hr); a is the sum of the surface area at the

266   headspace-medium interface (A_h) and total surface area of bubbles (A_b) (m^2); and δ is the thickness

267   of the diffusion layer (m). Using the δ values of 1 μm and 0.5 μm and other parameters specific to

268   the experimental setup of this study (Table 2), $k_L a$ values of 380 and 760 hr^{-1} were used in (Eqn.

269   13) to calculate [H_2]. The parameter $k_L a$ is unique to a specific experimental condition and

270   therefore varies between studies; however, the $k_L a$ range of 380 to 760 hr^{-1} falls reasonably within

271   the ranges reported previously (e.g., 0.16 h^{-1}, Pauss et al., 1990; 220–1540 h^{-1}, Jud et al., 1997).

272   Following are brief justifications of the values used in Table 2. D is a typical diffusion

273   coefficient for H_2 at 25 °C, 5.0×10^{-5} cm^2 sec^{-1} (Macpherson and Unwin, 1997). A_b is a function of

274   the geometry and the number of bubbles, which is determined by the relationship between the size

275   and residence time of bubbles and Q_{gas}. The upward velocity of bubbles for small bubbles (radius

276   < 0.1 cm) was calculated following Park et al. (2017). The residence time and total volume of

277   bubbles can be calculated for a known travel distance (i.e., height of the medium) and, from this,

278   the total area of bubbles, A_b, was calculated. Finally, the surface area at the headspace-medium

279   interface (A_h) is calculated from the reactor dimension.

280   2.3.8   Isotopologue flow network model

281   To examine the isotopologue data in this study with respect to the modeled $[H_2]$ values, we applied

282   the isotopologue flow network model adapted from Wang et al. (2015). The model calculates the

283   expected isotopologue compositions of CH_4 as well as the intermediate carbon-containing species.

284   During hydrogenotrophic methanogenesis (Eqn. 7), CO_2 is reduced to CH_4 via seven reactions and

285   six intermediate carbon species. Following Wang et al. (2015) and Cao et al. (2019), we reduced

286   the number of intermediate species to three by treating species with the same redox state as the

287   same pool (Figure 2A). Two sets of input parameters required for the model are reversibilities (φ)

288   for enzymatic reactions in the methanogenesis pathway and kinetic isotope effect (KIE) intrinsic

289   to enzymatic reactions.

290   The first set of input parameters, metabolic reversibility (φ), is the ratio of backward to

291   forward fluxes for an enzymatically-mediated reaction (Rees, 1973; Hayes, 2001). Previous

292   models have used a range of φ values between 0 and 1, where $\varphi = 0$ is fully kinetic (non-

293   equilibrium) and $\varphi = 1$ is fully reversible (equilibrium). Stolper et al., (2015) assumed $\varphi = 1$ for all

294   except for the last H-addition step, which was varied. Wang et al. (2015) implemented a gradual

295   and uniform departure from equilibrium ($\varphi = 1 \rightarrow 0$) for all H-addition steps. Cao et al. (2019)

296   tested binary cases, where φ is either 0 or 1 for each H-addition step. More recently, Gropp et al.

297   (2021) re-evaluated these three models with calculated equilibrium fractionation factors and

298   concluded that models in Wang et al. (2015) and Cao et al. (2019) can produce a range of carbon

299   isotope fractionation observed in the natural environment with certain combinations of φ. This

300   highlights the importance of φ, both in its degree of equilibrium at a given step and in its overall

301   variation among the four H-addition steps, in determining the outputs of isotopologue flow

302   network models. In this work, we parameterized φ values for the four H-addition steps as a function

303   of H_2 by assuming Michaelis–Menten kinetics, as described in Wang et al. (2015):

$$\varphi_n = 1 - \frac{[H_2]}{K_m + [H_2]} \qquad \text{(Eqn. 15)}$$

304   where n=1 to 4, representing the four H-addition steps (Figure 2A), and K_m is the effective half-

305   saturation constant. According to the model for the energy conservation of hydrogenotrophic

306   methanogenesis, the last step (reduction of methyl-CoM to CH_4) is exergonic and expected to be

307   less reversible compared to other steps (Thauer *et al.*, 2008; Thauer, 2011; Ono *et al.*, *in revision*).

308   We modeled differential reversibility by changing the K_m values (Eqn. 15) and compared

309   the following three cases:

310   1) equilibrium end-member scenario with a high K_m value of 10^4 M for all four reactions,

311   2) uniform reversibility scenario with a K_m value of 5×10^{-5} M for all four reactions, and

312   3) differential reversibility scenario with a K_m value of 5×10^{-5} M for the first three reactions

313   and a K_m value of 10^{-8} M (less reversible) for the last reaction.

314   The K_m value of 5×10^{-5} M approximates the experimentally determined K_m values for

315   hyperthermophilic methanogens (66 µM for three *Methanocaldococcus* species; Ver Eecke *et al.*,

316   2012). The lower K_m value of 10^{-8} M makes the last reversible step largely unidirectional down to

317   a low $[H_2]$ of $\sim10^{-8}$ M. For reference, the minimum threshold pH_2 estimated for pure cultures is

318   6.5 Pa (*ca.* 5×10^{-8} M at 25 °C), and the theoretical pH_2 at thermodynamic equilibrium for

319   hydrogenotrophic methanogenesis is 0.1 Pa (*ca.* 1×10^{-9} M at 25 °C) assuming $[CO_2]/[CH_4] = 1$

320   (Lovley, 1985; Thauer et al., 2008).

321   The values of KIEs are the second set of required input parameters for the model. KIEs are

322   experimentally determined only for the last reaction catalyzed by methyl-coenzyme M reductase

323   (Scheller et al., 2013). KIEs for other reactions are chosen to reproduce the kinetic end-member

324   solution and maintain the consistency with equilibrium fractionations (Appendix A; Table S1).

325   Equilibrium fractionation factors (α^{eq}) estimated by quantum mechanical calculation (Gropp et al.,

15

326   2021; Ono et al., 2021) constrain the model solution for the equilibrium end-member scenario

327   (Figure 2B). We use α^{eq} values estimated at 82 °C (experimental temperature for B.82 and F.82.80)

328   by Gropp et al. (2021) for fractionations between intermediates and $H_2O_{(g)}$ or $CO_{2,(g)}$. Then, α^{eq}

329   values against $H_2O_{(l)}$ were calculated from those against $H_2O_{(g)}$, using experimentally derived α

330   values between $H_2O_{(l)}$ and $H_2O_{(g)}$ (Horita and Wesolowski, 1994).

331   3   Results

332   3.1   Batch culture experiment

333   The trends observed with increasing $\delta^{13}C_{CH4}$ values and decreasing δD_{CH4} and $\Delta^{13}CH_3D$ values

334   (Table 3) were consistent with those previously reported for a batch culture experiment with *M.*

335   *bathoardescens* (Gruen et al., 2018). The carbon, hydrogen and clumped isotope fractionation

336   factors ($^{13}\alpha$, $^2\alpha$ and γ, respectively) calculated following Gruen et al. (2018) were comparable to

337   those reported previously: $^{13}\alpha$ of 0.98 (this study) compared to 0.97; $^2\alpha$ from 0.64 to 0.59 (this

338   study) compared to 0.69 to 0.57; and γ of 1.0005 (this study) compared to 1.0020 and 1.0032

339   (Supplementary Material, Figure S1D, S1E and S1F).

340   3.2   Fed-batch culture experiments (*M. bathoardescens*)

341   The growth of *M. bathoardescens* in fed-batch experiments were characterized by linear increase

342   in cell density (Supplementary Material, Figure S2A, S2D and S2G), consistent with previous

343   observations with *M. bathoardescens* in fed-batch experiments (Ver Eecke et al., 2012). For all

344   experiments, $^{13}\alpha$ decreased toward or went below that expected at CH_4-CO_2 equilibrium(Figure

345   3A4–3E4). $^2\alpha$ increased toward that expected at CH_4-H_2O equilibrium; however, the final $^2\alpha$ values

346   were still lower than that expected at equilibrium (Figure 3A5–3E5; Figure 4B). $\Delta^{13}CH_3D$ values

347   were low (range from –4.1 to 2.1‰) compared to equilibrium, indicating strong kinetic

348   fractionations, and decreased over time (Figure 3A6–3E6; Figure 4C). Detailed observations for

349   each experiment are described below.

350   During Experiment F.82.80, *M. bathoardescens* was grown at 82 °C and on 80% H_2. $^{13}\alpha$

351   decreased from 0.957 to 0.944 (Figure 3A4; Figure 4A), and $^2\alpha$ increased from 0.674 to 0.708

352   (Figure 3A5; Figure 4B). $\Delta^{13}CH_3D$ values ranged from 1.25 ± 0.48‰ to –0.29 ± 0.47‰ (Figure

353   3A6; Figure 4C). These $\Delta^{13}CH_3D$ values are lower than those expected at equilibrium (4.1‰ at

354   82 °C). Notably, the changes in $\Delta^{13}CH_3D$ were in the direction away from the values expected at

355   equilibrium, unlike $^{13}\alpha$ and $^2\alpha$ values that changed toward equilibrium values.

356   During Experiment F.60.80, *M. bathoardescens* was grown at a suboptimal temperature of

357   60 °C and on 80% H_2. $^{13}\alpha$ decreased from 0.982 to 0.964 (Figure 3B4; Figure 4A), and $^2\alpha$ increased

358   from 0.672 to 0.730 (Figure 3B5; Figure 4B). $\Delta^{13}CH_3D$ values ranged from 1.52 ± 0.58‰ to 0.06

359   ± 0.17‰ (Figure 3B6; Figure 4C). These $\Delta^{13}CH_3D$ values are lower than those expected at

360   equilibrium (4.6‰ at 60 °C) and also in the direction away from the values expected at equilibrium.

361   During Experiment F.82.25, *M. bathoardescens* was grown at 82 °C and on a lower xH_2 of 25%

362   H_2. Comparable to the observations in F.82.80, $^{13}\alpha$ decreased from 0.963 to 0.941 during F.82.25

363   (Figure 3C4; Figure 4A), and $^2\alpha$ increased from 0.668 to 0.699 (Figure 3C5; Figure 4B). $\Delta^{13}CH_3D$

364   values ranged from 1.15 ± 0.42‰ to –0.78 ± 0.73‰ (Figure 3C6; Figure 4C). The changes in

365     $\Delta^{13}CH_3D$ values during F.82.25 were also in the direction away from the values expected at

366   equilibrium, similar to the trends observed during F.82.80 and F.60.80.

367   The changes in bulk isotope values ($\delta^{13}C_{CO2}$, $\delta^{13}C_{CH4}$, δD_{H2O} and δD_{CH4}) during F.82.80,

368   F.60.80 and F.82.25 are reported in Table 4 and Supplementary Material, Figure S3. Note that, for

369   F.82.25, the absolute $\delta^{13}C_{CH4}$ values for F.82.25 are higher compared to those of F.82.80 because

370   different sources of CO_2 were used for the experiments.

371   3.3   Fed-batch culture experiments (*M. thermautotrophicus*)

372   The growth patterns of *M. thermautotrophicus* in fed-batch experiments were characterized by

373   distinct periods of exponential growth during the first 26 and 12 hours for F.65.20 (65 °C, 20% H_2)

374   and F.65.5 (65 °C, 5% H_2), respectively (Supplementary Material, Figure S4A and S4D). For

375   F.65.5, xH_2 in the supply gas was decreased from 5% to 1.6% after 55 hours. After decreasing the

376   xH_2 to 1.6%, the cell density remained relatively constant for the remainder of the experiment, and

377   xCH_4 and cs*MPR* decreased (Supplementary Material, Figure S4F; Table 5).

378    $^{13}\alpha$ decreased from 0.966 to 0.950 during F.65.20 and from 0.957 to 0.938 during F.65.5

379   (Figure 3D4 and 3E4; Figure 4A). $^2\alpha$ slightly increased during F.65.20 and did not change

380   significantly during F.65.5 (Figure 3D5 and 3E5; Figure 4B). $\Delta^{13}CH_3D$ values decreased over time,

381   moving away from that expected at equilibrium, as was observed in *M. bathoardescens*

382   experiments (Figure 3D6 and 3E6; Figure 4B). Notably, the magnitudes of depletion (i.e., low

383    $\Delta^{13}CH_3D$ values) observed during F.65.20 and F.65.5 are comparable to those observed during

384   batch experiments with mesophilic methanogens, which tend to produce lower $\Delta^{13}CH_3D$ values

385   compared to thermophilic methanogens (open *vs.* filled circles; Figure 4C). The changes in bulk

386   isotope values ($\delta^{13}C_{CO2}$, $\delta^{13}C_{DIC}$, $\delta^{13}C_{CH4}$, δD_{H2O} and δD_{CH4}) during F.65.20 and F.65.5 are reported

387   in Table 5 and Supplementary Material, Figure S5.

388   3.4   Dissolved H_2 in the liquid medium

389   The results of [H_2] calculations are shown in Figure 3. Overall, the results show undersaturation

390   in [H_2] with respect to headspace for high density and fast-growing cultures (Figure 3A1–4E1).

391 Media become more undersaturated over time (i.e., at higher cell density; Figure 3A2–3E2) due to

392 the increase in total H_2 consumption rate, which corresponds with the increase in *MPR* (Figure

393 3A3–3E3). The difference between the maximum $[H_2]^{eq}$ and minimum $[H_2]$ values (with lower

394 k_La) was the largest, between 2-fold and >10-fold, at the highest temperature (82 °C; F.82.80 and

395 F.82.25), whereas the difference was <2-fold at lower temperatures of 65°C and 60°C. The lower

396 range of $[H_2]$ was calculated using the minimum k_La value required to avoid a negative $[H_2]$ in all

397 experiments (350 h^{-1}), and the higher range of $[H_2]$ was calculated with a k_La value of 350 h^{-1},

398 twice as much as the minimum value (Figure 3A3–3E3).

399 3.5   Isotopologue flow network model

400 The equilibrium end-member scenario shows uniform values across the $[H_2]$ range that correspond

401 to values expected at equilibrium (–51‰ for $\delta^{13}C$, –151‰ for δD and 6‰ for $\Delta^{13}CH_3D$ at 82 °C,

402 yellow dotted line; Figure 5). The isotope values change as a function of $[H_2]$ in the uniform

403 reversibility and differential reversibility scenarios (red dashed line and blue solid line,

404 respectively; Figure 5). The $\delta^{13}C$ and $\Delta^{13}CH_3D$ profiles show significant difference between

405 uniform and differential reversibility scenarios; in the differential reversibility scenario, $\delta^{13}C$ and

406 $\Delta^{13}CH_3D$ values decrease to local minima at a $[H_2]$ range between the two K_m values assigned for

407 reversibility terms (i.e., 5×10^{-5} M for φ_{1-3}; 10^{-8} M for φ_4), and values increase toward the

408 equilibrium values when all four steps become reversible ($[H_2] \lesssim 10^{-7}$ M) (Figure 5A and 5C).

409 The low $\delta^{13}C$ values between the two K_m values are less than the value expected for equilibrium.

410 In the Discussion section below, we provide further interpretations for the patterns of isotope

411 fractionation factors ($^{13}\alpha$, $^{2}\alpha$) and clumped isotopologue abundance ($\Delta^{13}CH_3D$) observed during

412 fed-batch experiments in this study in light of $[H_2]$ and isotopologue flow network model results.

4   Discussion

Our results—from combined analyses of $\delta^{13}C_{CO2}$, $\delta^{13}C_{CH4}$, δD_{H2O}, δD_{CH4} and $\Delta^{13}CH_3D$—confirm previous observations that carbon isotope fractionation increases with decreasing pH_2 (Penning et al., 2005; Londry et al., 2008; Okumura et al., 2016; Topçuoğlu et al., 2019; Nguyen et al., 2020) and shed some new light on the behavior of hydrogen isotope and clumped isotopologue systems at different growth phases and $[H_2]$. The observed values of consistently low δD_{CH4} and $\Delta^{13}CH_3D$ (relative to equilibrium) suggest primarily kinetic fractionations for hydrogen and clumped isotope systems under our experimental conditions. However, the apparent decrease in $\Delta^{13}CH_3D$ values (i.e., further departure from equilibrium) for later growth phase and low $[H_2]$ was unexpected and contrasts previous model predictions based on the differential reversibility hypothesis (e.g., Stolper et al., 2015; Wang et al., 2015). Using the modeled values of $[H_2]$ in the fed-batch system and results of isotopologue flow network model, we discuss the observed patterns of $^{13}\alpha$ (section 4.1); $^2\alpha$ and $\Delta^{13}CH_3D$ (section 4.2); limitations of the model and broader implications for interpreting the isotopic signatures of natural methane samples (section 4.3).

4.1   High cell density during stationary growth phase leads to low $[H_2]$ and higher than equilibrium carbon isotope fractionations

The magnitude of carbon isotope fractionation is higher (lower $^{13}\alpha$ values) for later growth phase within a single experiment and at lower xH_2 across experiments (Figure 3A4–3E4; Figure 4A). The decrease in $^{13}\alpha$ coincides with the transition from exponential phase to stationary phase for *M. thermautotrophicus* (Figure 3D2 and 3E2) or later linear growth for *M. bathoardescens* (Figure 3A2–3C2). Our observation is consistent with previous culture studies that reported increasing carbon isotope fractionation as a function of growth phase (Botz et al., 1996; Valentine et al., 2004)

435   and experiments with lower pH$_2$ (Valentine et al., 2004; Londry et al., 2008; Okumura et al., 2016;

436   Topçuoğlu et al., 2019; Nguyen et al., 2020). Some studies have also reported larger than

437   equilibrium isotope fractionation (e.g., Botz et al., 1996; Valentine et al., 2004; Penning et al.,

438   2005; Okumura et al., 2016; Topçuoğlu et al., 2019), similar to the observations in this study (e.g.,

439   F.82.80, F.82.25 and F.65.5 in Figure 3A4–3E4 and Figure 4A).

440   In addition to causing physiological changes, later growth phase with high cell density

441   leads to low [H$_2$] due to the increase in total H$_2$ consumption rate. The decrease in [H$_2$] at high cell

442   density is important to consider for the hydrogenotrophic methanogenesis reaction because of its

443   4:1 H$_2$:CH$_4$ stoichiometry (Eqn. 7) and poor solubility of H$_2$. While the dissolved concentrations

444   of highly soluble gases (e.g., CO$_2$) can be close to equilibrium with the headspace, the dissolved

445   concentrations of poorly soluble gases (e.g., H$_2$ and CH$_4$) can be far away from equilibrium with

446   the gas phase. Higher partial pressure of water vapor at saturation (pH$_2$O$_{sat}$) in the reactor

447   headspace during (hyper)thermophilic incubations should also be considered (Eqn. 11), as it would

448   further lower the [H$_2$] in liquid media. The observed linear growth for *M. bathoardescens* (Figure

449   3A2–3C2) suggests that growth and methane production rates were limited by the supply

450   (=dissolution) rate of H$_2$.

451   Accurate measurement of [H$_2$] for methanogenic media can be challenging. Previous

452   studies measured [H$_2$] for fed-batch reactors or chemostats by sampling liquid media into serum

453   vials and measuring pH$_2$ in the headspace (e.g., Ver Eecke et al., 2012; Stewart et al., 2016;

454   Topçuoğlu et al., 2018, 2019). For example, Topçuoğlu et al. (2019) reported [H$_2$] values (prior to

455   inoculation) of 82 ± 2 and 21 ± 6 µM for high and low H$_2$ experiments, respectively. These values

456   are lower and higher than the saturation concentrations (516 and 10 µM) based on the dry H$_2$

457   mixing ratios of 86.6 and 1.6% for high and low H$_2$ experiments, respectively. Here, high pH$_2$O$_{sat}$

458   at higher temperatures (0.51 bars at 82°C) can explain lower [H_2] compared to calculations for dry

459   headspace. Higher than saturation [H_2] values may indicate entrainment of H_2 microbubbles in

460   addition to dissolved H_2 (e.g., McGinnis et al., 2015). After inoculation, microbial consumption

461   of H_2 would affect the steady state dissolved concentrations of gases in the liquid due to relatively

462   slow rate of H_2 dissolution (Eqn. 12). For example, in anaerobic fermentors where H_2 is produced

463   by microbial processes, the liquid-to-gas mass transport limit resulted in as much as 80 times

464   oversaturation of H_2 compared to the headspace gas (Pauss et al., 1990). On the other hand, in

465   chemostat cultures where methanogens consume H_2 (i.e., gas-to-liquid transport), the dissolved H_2

466   concentration was found to be 10 times lower than the saturation with respect to gas phase (Jud et

467   al., 1997). Because methanogens use dissolved form of H_2, we estimated [H_2] under each

468   experimental condition to assess the effect of the dissolved H_2 concentration on isotope

469   fractionation.

470   As shown in Figure 6A, the modeled [H_2] range under our experimental conditions (*ca.* 7

471   to 410 µM) is lower than the [H_2] range expected for typical batch cultures (e.g., 0.6 to 1.2 mM

472   for 1 to 2 bars of 80% H_2 headspace) and partially overlaps with the [H_2] range found in cow rumen

473   (0.1 to 50 µM; Smolenski and Robinson, 1988; Janssen, 2010, and references therein; Wang et al.,

474   2015); but it is higher than the [H_2] range found in typical freshwater (5 to 75 nM; Robinson and

475   Tiedje, 1982; Conrad et al., 1985; Conrad et al., 1987; Kuivila et al., 1989) and marine sediments

476   (2 to 60 nM; Lin et al., 2012). In the differential reversibility scenario for the isotopologue flow

477   network model, $\delta^{13}C$ values decrease with a decrease in [H_2] for [H_2] <1 mM (between 10^{-6} and

478   10^{-3} M; Figure 5A). This is consistent with the decreasing $^{13}\alpha$ values observed during fed-batch

479   experiments with a decrease in [H_2] (due to increase in cell density) or xH_2 (mixing ratios for

480   different experiments) for the modeled [H_2] range between 7 and 410 µM (between 7×10^{-6} and

481 4×10^{-4} M; Figure 6B). In addition, the $^{13}\alpha$ values during the fed-batch experiment conducted at

482 82 °C and 80% H_2 (F.82.80; $^{13}\alpha = 0.95 \pm 0.01$; Table 4, Figure 4A) were lower compared to the

483 $^{13}\alpha$ value for batch experiment conducted at the same temperature and initial xH_2 (B.82.80; $^{13}\alpha =$

484 0.98; Supporting Information, Figure S1D). Considering that $[H_2]$ in batch cultures at high

485 headspace pressure (1 to 2 bars) and xH_2 (80%) can reach millimolar levels (0.6 to 1.2 mM; Figure

486 6A), the difference in $^{13}\alpha$ values observed between fed-batch and batch experiments is also

487 consistent with the overall correlation between low $^{13}\alpha$ and low $[H_2]$.

488   Besides the general correlation between low $[H_2]$ and larger carbon isotope fractionation,

489 our isotopologue flow network model reproduced the large carbon isotope fractionation (larger

490 than equilibrium) observed during later growth phases in the differential reversibility scenario

491 (Figure 5A). When $[H_2]$ is between 5×10^{-5} and 10^{-8} M (i.e., two K_m values assigned for φ_1 to φ_3

492 and φ_4, respectively), reactions up to CH_3-CoM are largely reversible (φ_1 to $\varphi_3 \simeq 1$). As a result,

493 $\delta^{13}C$ of the methyl group of CH_3-CoM approaches to equilibrium value ($-52‰$ at 82°C; Gropp et

494 al., 2021). The reversibility of the last step is relatively low above 10^{-8} M H_2 in our model, and

495 this step can result in kinetic isotope fractionation of up to $-40‰$ ($^{13}\alpha = 0.96 \pm 0.01$, assayed at

496 60 °C; Scheller et al., 2013). Accordingly, the maximum overall fractionation of $\sim-92‰$ ($-52 -$

497 40‰) can be achieved when the first three steps are fully reversible (φ_1 to $\varphi_3 \simeq 1$) and the last step

498 is fully kinetic ($\varphi_4 \simeq 0$). This is consistent with the minimum $^{13}\alpha$ value (0.908, or fractionation of

499 $-92‰$) in the differential reversibility scenario simulated at 60 °C in our study (yellow solid line;

500 Figure 6B). At much lower $[H_2]$ (i.e., $<10^{-8}$ M), the last step of methanogenesis becomes reversible

501 and equilibrium fractionation is expected ($-57‰$ at 60 °C, $-51‰$ at 82 °C; Figure 6B).

502 4.2 Differential reversibility can explain the observed hydrogen and clumped isotopologue

503   systematics

504 Previous culture studies have so far exclusively produced non-equilibrium hydrogen isotope

505 fractionation (Valentine et al., 2004; Yoshioka et al., 2008; Hattori et al., 2012; Kawagucci et al.,

506 2014; Stolper et al., 2015; Okumura et al., 2016; Gruen et al., 2018). In this study, hydrogen isotope

507 system similarly indicated significant departure from equilibrium ($^2\alpha = 0.69 \pm 0.02$, Figure 3A5–

508 3E5, Figure 4B *vs.* $^2\alpha^{eq} = 0.81$ at 60 °C and 0.82 at 82 °C). In the differential reversibility scenario

509 (blue solid line; Figure 5B) δD values slightly increase for $[H_2] \geq 10^{-5}$ M, stay relatively constant

510 for the $[H_2]$ range between 10^{-5} M and 10^{-8} M, and significantly increase toward equilibrium value

511 for $[H_2] \leq 10^{-8}$ M (note that the two inflection points in the δD profile occur around the two K_m

512 values assigned for φ_1 to φ_3 and φ_4, respectively). This is consistent with our isotope data for fed-

513 batch experiments for the modeled $[H_2]$ range between 7 and 410 µM (between 7×10^{-6} and $4 \times 10^{-}$

514 ^{4} M), where relatively constant $^2\alpha$ values were observed (Figure 6B).

515   The relatively constant $^2\alpha$ for modeled $[H_2]$ between 10^{-5} M and 10^{-8} M in the differential

516 reversibility scenario (Figure 5B) and observed in our experiments (Figure 6C) can be explained

517 with a large KIE associated with the last step of methanogenesis (CH_3-CoM to CH_4 reduction;

518 reaction 4, Figure 2A). As described above in section 4.1, reactions up to CH_3-CoM are reversible

519 (φ_1 to $\varphi_3 \simeq 1$) in the differential reversibility scenario for the $[H_2]$ range between 5×10^{-5} and 10^{-8}

520 M. Consequently, the three H atoms in the methyl group of CH_3-CoM are isotopically equilibrated

521 with the surrounding water ($\delta D_{CH3-CoM} = -122$‰ at 82 °C; Gropp et al., 2021). The reversibility

522 of the last step is relatively low at $[H_2] \geq 10^{-8}$ M in our model, and this step can result in large

523 kinetic isotope fractionation. For reference, Scheller et al., (2013) reported experimentally

524 determined values of primary KIE (k_H/k_D) of 2.44 (i.e., $^{2,P}\alpha$ of 0.41) and secondary KIE of 1.17

525   (i.e., $^{2,S}\alpha$ of 0.85) at 60 °C for the last step in reverse direction. The addition of the last H atom

526   from water (e.g., $\delta D_{H2O} = -50‰$) to the equilibrated CH_3-CoM with the $^{2,P}\alpha$ and $^{2,S}\alpha$ values above

527   would result in the final δD_{CH4} of $-343‰$ (= [¾ · ($-122/1000+1$) · (0.85) + ¼ · ($-50/1000+1$) ·

528   (0.41)] – 1), which is comparable to the range observed in our experiments ($-339 \pm 34‰$; Table 4;

529   Table 5).

530   These experimental and model results together suggest that the persistent non-equilibrium

531   signatures observed for hydrogen isotope system in this study and previous studies are results of

532   differential reversibility with a less reversibility (larger KIE) at the last H-addition step. It follows

533   that, in our model setup, hydrogen isotope fractionation approaches to equilibrium values at sub-

534   μM ranges of $[H_2]$ (solid line, Figure 6C). Future experiments with direct measurements and

535   precise control of $[H_2]$ (e.g., continuous cultures) at sub-μM levels are needed to validate this

536   hypothesis.

537   Similar to $^2\alpha$ values, $\Delta^{13}CH_3D$ values were depleted and also indicated significant departure

538   from equilibrium; unlike in hydrogen isotope system, however, a distinct pattern of decreasing

539     $\Delta^{13}CH_3D$ values was observed for clumped isotope system (Figure 3A6–3E6; Figure 6D). This is

540   in sharp contrast with previous isotope model results that suggest a positive correlation between

541   the overall metabolic reversibility and $\Delta^{13}CH_3D$ (e.g., Stolper et al., 2015; Wang et al., 2015). In

542   this case, more reversibility would result in the increase of $\Delta^{13}CH_3D$ toward the value expected at

543   internal isotopologue equilibrium (ca. 4‰ at 82 °C). This unexpected pattern $\Delta^{13}CH_3D$ values was

544   reproduced in the differential reversibility scenario, with a distinct decrease in $\Delta^{13}CH_3D$ values for

545   the $[H_2]$ range between ca. 5×10^{-4} and 10^{-7} M (blue solid line, Figure 5C). Note that the two

546   inflection points in the $\Delta^{13}CH_3D$ profile occur around the two assigned K_m values of 5×10^{-5} and

547   10^{-8} M for φ_1 to φ_3 and φ_4, respectively. The effect of assigned K_m values on the $\Delta^{13}CH_3D$ profile

548   was evident from sensitivity test results (Supplemental Material, Figure S6). The K_m value of

549   5×10^{-5} M for φ_1 to φ_3 resulted in the best fit to the $\Delta^{13}CH_3D$ values measured from the fed-batch

550   experiments in this study (e.g., panel C *vs*. panels A, B, D or E; Supplemental Material, Figure S6).

551   This is likely not a coincidence, given that the experimentally determined K_m value for

552   hyperthermophilic methanogens is close to the assigned value (6.6×10^{-5} M for three

553   *Methanocaldococcus* species; Ver Eecke *et al.*, 2012). Because our experiments were done at the

554   modeled $[H_2]$ range between 7 and 410 μM, we cannot empirically assess the fit of the lower K_m

555   value assigned for φ_4 in the differential reversibility scenario. For example, varying the $[H_2]$ value

556   for φ_4 between 10^{-10} and 10^{-6} M has negligible effect on the $\Delta^{13}CH_3D$ profile for $[H_2] \geq 10^{-6}$ M

557   (panels F–J; Supplemental Material, Figure S6). Future experiments at sub-μM levels of $[H_2]$ are

558   needed to properly determine the threshold K_m value for the last step of methanogenesis (which

559   may depend on the species) that would equilibrate $\Delta^{13}CH_3D$ signatures. However, the K_m value of

560   10^{-8} M for φ_4 used in this study is reasonable, considering that equilibrium $\Delta^{13}CH_3D$ signatures in

561   microbial methane have been found in marine sediments where the typical $[H_2]$ range is between

562   2 and 60 nM (Lin et al., 2012; Figure 6A).

563   Another characteristic pattern of the clumped isotope system observed in our experiments

564   was significant depletion in $^{13}CH_3D$ with anti-clumped (negative) $\Delta^{13}CH_3D$ values at low $[H_2]$ or

565   xH_2 (Figure 3A6–3E6; Figure 6D). The differential reversibility scenario shown in Figure 5C and

566   Figure 6D successfully reproduces not only the decreasing trend but also anti-clumped $\Delta^{13}CH_3D$

567   values that fits the range of $\Delta^{13}CH_3D$ values observed in this study (minimum of –4.1‰).

568   Sensitivity test results indicated that secondary clumped isotope fractionation of ≥ 6‰ (i.e., $^S\gamma \geq$

569   0.994) is required to produce a distinct decreasing pattern with negative $\Delta^{13}CH_3D$ values at $[H_2] \geq$

570   10^{-5} M (i.e., lower end of our experimental range) (panels A–F; Supplemental Material, Figure

571 S7). The $^{S}\gamma$ value of 0.990 (i.e., 10‰ secondary clumped isotope fractionation) resulted in the

572 profile that best fits both the decreasing trend and magnitude of depletion in measured $\Delta^{13}CH_3D$

573 values (Figure 5C, Figure 6D). Varying the magnitude of primary clumped isotope fractionation

574 ($^{P}\gamma$) without any secondary isotope fractionation ($^{S}\gamma=1$) did not reproduce the observed patterns in

575 $\Delta^{13}CH_3D$ (panels G–L; Supplemental Material, Figure S7).

576 4.3   Limitations of the isotopologue flow network model and implications for interpreting the

577   isotope signatures of natural methane samples

578 While we explored three different cases—including the differential reversibility scenario—for the

579 isotopologue flow network model, there is much complexity associated with the biochemical inner

580 workings of methanogenesis that is not captured in the model. The model uses a constant KIE

581 value per H-addition step, assuming that each step is catalyzed by the same enzyme across the

582 range of [H_2] examined in this study (10^{-9} to 10^{-2} M). This may not be true for H-addition steps

583 that can be catalyzed by more than one enzyme (i.e., isoenzymes). There are at least two sets of

584 isoenzymes known to catalyze the second and fourth H-addition steps during hydrogenotrophic

585 methanogenesis. The fourth step of methanogenesis (the reduction of methenyl-H_4MPT^+ to

586 methylene-H_4MPT) involves either the oxidation of H_2 or the oxidation of the reduced form of F_{420}

587 ($F_{420}H_2$), where the former is catalyzed by H_2-forming N^5,N^{10}-methylene-H_4MPT dehydrogenase

588 (Hmd) and the latter is catalyzed by F_{420}-dependent N^5,N^{10}-methylene-H_4MPT dehydrogenase

589 (Fmd) (von Bünau et al., 1991; Reeve et al., 1997). Previous studies have shown that Mtd increases

590 in expression, relative to Hmd, under H_2 limitation (Reeve et al., 1997; Hendrickson et al., 2007;

591 Topçuoğlu et al., 2019). The isoenzyme switching from Hmd to Mtd under H_2 limitation has been

592 suggested to allow a greater expression of carbon isotope fractionation (Valentine et al., 2004) and

593 may apply for hydrogen and clumped isotope systems as well.

594   Another set of isoenzymes, MCR I and MCR II (sometimes referred to as MR I and MR

595   II), catalyzes the fourth and last H-addition steps of hydrogenotrophic methanogenesis (Pihl et al.,

596   1994; Reeve et al., 1997). The relative abundances of MCR I and MCR II have been shown to be

597   determined largely by growth phase, where MCR II is preferentially expressed during exponential

598   phase and MCR I during linear or stationary phase (Rospert et al., 1990; Bonacker et al., 1992;

599   Pihl et al., 1994). Whether distinct KIEs are associated with these isoenzymes remains unclear;

600   however, considering that MCR I and MCR II have different substrate affinities (i.e., K_m values

601   for CH_3-S-CoM and H-S-HTP) and catalytic rates (Bonacker et al., 1993), it is possible that these

602   isoenzymes for the rate-limiting step of last H-addition impart distinct KIEs. Future studies

603   combining a proteomic or transcriptomic approach and isotope analyses are needed to evaluate the

604   effect of isoenzyme switching on isotope fractionation during hydrogenotrophic methanogenesis.

605   Despite the limitations mentioned above, insights gained from the empirical relationships

606   among bulk ($^{13}\alpha$, $^{2}\alpha$) and clumped ($\Delta^{13}CH_3D$) isotope systems investigated in this study help us

607   better interpret the isotope signatures in natural samples of methane. Our experimental and model

608   results show that the nuances of isotope fractionation at a given time point warrant further

609   consideration of physiological state and the amount of H_2 available for methanogens in the

610   dissolved form. For example, rather than characterizing carbon isotope values with either an

611   equilibrium or kinetic end-member signature, one would need to consider the large carbon isotope

612   fractionation (larger than equilibrium) that can result from differential reversibility at an

613   intermediate range of [H_2] (between 10^{-5} M and 10^{-8} M under our experimental conditions; Figure

614   5A).

615   Clumped isotope results also suggest that low $\Delta^{13}CH_3D$ values are not necessarily

616   associated with specific growth temperatures or metabolic pathways (e.g., hydrogenotrophic *vs*.

617 acetoclastic *vs*. methylotrophic). In studies where hydrogenotrophic species were grown on

618 H_2/CO_2 at different temperatures, mesophilic cultures in general were associated with larger

619 depletion in $\Delta^{13}CH_3D$ compared to thermophilic cultures (Figure 4C; Stolper et al., 2015; Wang et

620 al., 2015; Gruen et al., 2018). In studies where methanogens were grown on different substrates

621 using different biochemical pathways, methylotrophic and acetoclastic cultures in general carried

622 more depleted $\Delta^{13}CH_3D$ (and $\Delta^{12}CH_2D_2$) signatures (Young et al., 2017; Gruen et al., 2018). The

623 wide range of $\Delta^{13}CH_3D$ values (–4.1 to 2.1‰) observed in this study, where all cultures were

624 grown under hyperthermophilic and hydrogenotrophic conditions, suggests that the magnitude of

625 depletion in clumped isotopologues is not always associated with growth temperatures or

626 methanogenic pathways.

627 ## 5   Conclusion

628 We cultured two different species of methanogens, *Methanocaldococcus bathoardescens* and

629 *Methanothermobacter thermautotrophicus* (ΔH), in batch and fed-batch systems and measured the

630 $\delta^{13}C$ and δD of the substrates (CO_2 and H_2O) as well as the $\delta^{13}C$, δD and $\Delta^{13}CH_3D$ of the product

631 (CH_4). The results of the fed-batch experiments confirm previous observations, where carbon

632 isotope fractionation ($^{13}\alpha = 0.96 \pm 0.02$) approaches and often exceed the magnitude expected at

633 CH_4-CO_2 equilibrium (e.g., Botz et al., 1996; Valentine et al., 2004; Penning et al., 2005; Okumura

634 et al., 2016; Topçuoğlu et al., 2019), while hydrogen isotope fractionation remains significantly

635 larger ($^2\alpha = 0.67 \pm 0.01$) than that expected at CH_4-H_2O equilibrium (Figure 4). The observed low

636 $\Delta^{13}CH_3D$ values indicate kinetic isotope effects, with an apparent decrease in $\Delta^{13}CH_3D$ values with

637 decreasing pH_2. The isotopologue flow network model presented showed our observations—large

638 carbon isotope fractionation, depleted hydrogen isotope signatures, and distinct decreasing

639 $\Delta^{13}CH_3D$ values with decreasing pH_2—can be explained by differential reversibility, in which the

640   last step of methanogenesis is less reversible compared to the preceding three H-addition reactions.

641   In addition, including secondary clumped KIE in the model reproduced the magnitude of depletion

642   in $\Delta^{13}CH_3D$ values observed in our experiments. Future studies focusing on controlled H_2

643   limitation experiments at sub-μM concentrations and conducting proteomic or transcriptomic

644   analyses in parallel may improve our interpretations of the bulk and clumped isotope signatures

645   used for methane source identification.

646

647   **Acknowledgment**

655

656   **Appendix A. Supplementary Material**

657   Research Data that supports this research publication can be found in the Supplementary Material

658   at [Link].

659

660 **References**

661 Balabane M., Galimov E., Hermann M. and Létolle R. (1987) Hydrogen and carbon isotope

662   fractionation during experimental production of bacterial methane. *Org. Geochem.* **11**, 115–

663   119.

664 Baldassare F. J., McCaffrey M. A. and Harper J. A. (2014) A geochemical context for stray gas

665   investigations in the northern Appalachian Basin: Implications of analyses of natural gases

666   from Neogene-through Devonian-age strata. *Am. Assoc. Pet. Geol. Bull.* **98**, 341–372.

667 Belyaev S. S., Wolkin R., Kenealy W. R., DeNiro M. J., Epstein S. and Zeikus J. G. (1983)

668   Methanogenic Bacteria from the Bondyuzhskoe Oil Field: General Characterization and

669   Analysis of Stable-Carbon Isotopic Fractionation. *Appl. Environ. Microbiol.* **45**, 691–697.

670 Bonacker L. G., Baudner S., Mörschel E., Böcher R. and Thauer R. K. (1993) Properties of the

671   two isoenzymes of methyl-coenzyme M reductase in Methanobacterium

672   thermoautotrophicum. *Eur. J. Biochem.* **217**, 587–595.

673 Bonacker L. G., Baudner S. and Thauer R. K. (1992) Erratum: Differential expression of the two

674   methyl-coenzyme M reductases in Methanobacterium thermoautotrophicum as described

675   immunochemically via isoenzyme-specific antisera (European Journal of Biochemistry,

676   Vol. 206, No. 1). *Eur. J. Biochem.* **207**, 1129.

677 Botz R., Pokojski H.-D., Schmitt M. and Thomm M. (1996) Carbon isotope fractionation during

678   bacterial methanogenesis reduction. **25**, 255–262.

679 von Bünau R., Zirngibl C., Thauer R. K. and Klein A. (1991) Hydrogen-forming and coenzyme-

680   F420-reducing methylene tetrahydromethanopterin dehydrogenase are genetically distinct

681   enzymes in Methanobacterium thermoautotrophicum (Marburg). *Eur. J. Biochem.* **202**,

682   1205–1208.

683 Cao X., Bao H. and Peng Y. (2019) A kinetic model for isotopologue signatures of methane

684   generated by biotic and abiotic CO2 methanation. *Geochim. Cosmochim. Acta* **249**, 59–75.

685 Chabab S., Théveneau P., Coquelet C., Corvisier J. and Paricaud P. (2020) Measurements and

686   predictive models of high-pressure H2 solubility in brine (H2O+NaCl) for underground

687   hydrogen storage application. *Int. J. Hydrogen Energy* **45**, 32206–32220.

688 Conrad R., Goodwin S. and Zeikus J. G. (1987) Hydrogen metabolism in a mildly acidic lake

689   sediment (Knaack Lake). *FEMS Microbiol. Lett.* **45**, 243–249.

690 Conrad R., Phelps T. J. and Zeikus J. G. (1985) Gas metabolism evidence in support of the

691   juxtaposition of hydrogen-producing and methanogenic bacteria in sewage sludge and lake

692   sediments. *Appl. Environ. Microbiol.* **50**, 595–601.

693 Coplen T. B. (2011) Guidelines and recommended terms for expression of stable-isotope-ratio

694   and gas-ratio measurement results. *Rapid Commun. Mass Spectrom.* **25**, 2538–2560.

695 Douglas P. M. J., Stolper D. A., Eiler J. M., Sessions A. L., Lawson M., Shuai Y., Bishop A.,

696   Podlaha O. G., Ferreira A. A., Santos Neto E. V., Niemann M., Steen A. S., Huang L.,

697   Chimiak L., Valentine D. L., Fiebig J., Luhmann A. J., Seyfried W. E., Etiope G., Schoell

698   M., Inskeep W. P., Moran J. J. and Kitchen N. (2017) Methane clumped isotopes: Progress

699   and potential for a new isotopic tracer. *Org. Geochem.* **113**, 262–282. Available at:

700   https://doi.org/10.1016/j.orggeochem.2017.07.016.

701 Ver Eecke H. C., Butterfield D. A., Huber J. A., Lilley M. D., Olson E. J., Roe K. K., Evans L.

702   J., Merkel A. Y., Cantin H. V. and Holden J. F. (2012) Hydrogen-limited growth of

703   hyperthermophilic methanogens at deep-sea hydrothermal vents. *Proc. Natl. Acad. Sci. U.

704   S. A.* **109**, 13674–13679.

705 Etiope G. and Sherwood Lollar B. (2013) Abiotic methane on earth. *Rev. Geophys.* **51**, 276–299.

706   Flores R. M., Rice C. A., Stricker G. D., Warden A. and Ellis M. S. (2008) Methanogenic

707   pathways of coal-bed gas in the Powder River Basin, United States: The geologic factor.

708   *Int. J. Coal Geol.* **76**, 52–75.

709   Fuchs G., Moll J., Scherer P. and Thauer R. (1979a) Activity, acceptor specificity and function

710   of hydrogenase in Methanobacterium thermoautotrophicum. *Hydrog. Their Catal. Act.,*

711   *Struct. Funct., Work. Meet.*, 83–92.

712   Fuchs G., Thauer R., Ziegler H. and Stichler W. (1979b) Carbon Isotope Fractionation by

713   Methanobacterium thermoautotrophicum. **9**, 135–139.

714   Games L. M. and Hayes J. M. (1978) Methane-producing bacteria : natural frac ~ onatio ~ s of

715   tbe stable carbon isotopes. **42**, 1295–1297.

716   Gonzalez Y., Nelson D. D., Shorter J. H., McManus J. B., Dyroff C., Formolo M., Wang D. T.,

717   Western C. M. and Ono S. (2019) Precise Measurements of 12CH2D2 by Tunable Infrared

718   Laser Direct Absorption Spectroscopy. *Anal. Chem.* **91**, 14967–14974.

719   Gropp J., Iron M. A. and Halevy I. (2021) Theoretical estimates of equilibrium carbon and

720   hydrogen isotope effects in microbial methane production and anaerobic oxidation of

721   methane. *Geochim. Cosmochim. Acta* **295**, 237–264. Available at:

722   https://doi.org/10.1016/j.gca.2020.10.018.

723   Gruen D. S., Wang D. T., Ko M., Stewart L. C., Goldhammer T., Holden J. F., Hinrichs K. and

724   Ono S. (2018) ScienceDirect Experimental investigation on the controls of clumped

725   isotopologue and hydrogen isotope ratios in microbial methane. **237**, 339–356.

726   Hattori S., Nashimoto H., Kimura H., Koba K., Yamada K., Shimizu M., Watanabe H., Yoh M.

727   and Yoshida N. (2012) Hydrogen and carbon isotope fractionation by thermophilic

728   hydrogenotrophic methanogens from a deep aquifer under coculture with fermenters.

729   *Geochem. J.* **46**, 193–200.

730   Hayes J. M. (2001) Fractionation of carbon and hydrogen isotopes in biosynthetic processes.

731   *Rev. Mineral. Geochemistry* **43**, 225–277.

732   Haynes W. M., Lide D. R. and Bruno T. J. (2016) *CRC handbook of chemistry and physics: a*

733   *ready-reference book of chemical and physical data*. 97th Editi., CRC Press, Boca Raton,

734   Florida.

735   Hendrickson E. L., Haydock A. K., Moore B. C., Whitman W. B. and Leigh J. A. (2007)

736   Functionally distinct genes regulated by hydrogen limitation and growth rate in

737   methanogenic Archaea. **2007**.

738   Horibe Y. and Craig H. (1995) D/H fractionation in the system methane-hydrogen-water.

739   *Geochim. Cosmochim. Acta* **59**, 5209–5217.

740   Horita J. (2001) Carbon isotope exchange in the system CO2-CH4 at elevated temperatures.

741   *Geochim. Cosmochim. Acta* **65**, 1907–1919.

742   Horita J. and Wesolowski D. J. (1994) Horita and Wesolowski 1994. *Geochim. Cosmochim. Acta*

743   **58**, 1–13.

744   Janssen P. H. (2010) Influence of hydrogen on rumen methane formation and fermentation

745   balances through microbial growth kinetics and fermentation thermodynamics. *Anim. Feed*

746   *Sci. Technol.* **160**, 1–22.

747   Jud G., Schneider K. and Bachofen R. (1997) The role of hydrogen mass transfer for the growth

748   kinetics of Methanobacterium thermoautotrophicum in batch and chemostat cultures. *J. Ind.*

749   *Microbiol. Biotechnol.* **19**, 246–251.

750   Kawagucci S., Kobayashi M., Hattori S., Yamada K., Ueno Y., Takai K. and Yoshida N. (2014)

751   Hydrogen isotope systematics among H2–H2O–CH4 during the growth of the

752   hydrogenotrophic methanogen Methanothermobacter thermautotrophicus strain ΔH.

753   *Geochim. Cosmochim. Acta* **142**, 601–614.

754   Krzycki J. A., Kenealy W. R., DeNiro M. J. and Zeikus J. G. (1987) Stable Carbon Isotope

755   Fractionation by Methanosarcina barkeri during Methanogenesis from Acetate, Methanol,

756   or Carbon Dioxide-Hydrogen. *Appl. Environ. Microbiol.* **53**, 2597–2599.

757   Kuivila K. M., Murray J. W., Devol A. H. and Novelli P. C. (1989) Methane production, sulfate

758   reduction and competition for substrates in the sediments of Lake Washington. *Geochim.*

759   *Cosmochim. Acta* **53**, 409–416.

760   Lin Y. S., Heuer V. B., Goldhammer T., Kellermann M. Y., Zabel M. and Hinrichs K. U. (2012)

761   Towards constraining H2 concentration in subseafloor sediment: A proposal for combined

762   analysis by two distinct approaches. *Geochim. Cosmochim. Acta* **77**, 186–201.

763   Londry K. L., Dawson K. G., Grover H. D., Summons R. E. and Bradley A. S. (2008) Stable

764   carbon isotope fractionation between substrates and products of Methanosarcina barkeri.

765   *Org. Geochem.* **39**, 608–621.

766   Lovley D. R. (1985) Minimum threshold for hydrogen metabolism in methanogenic bacteria.

767   *Appl. Environ. Microbiol.* **49**, 1530–1531.

768   Macpherson J. V and Unwin P. R. (1997) Determination of the Diffusion Coefficient of

769   Hydrogen in Aqueous Solution Using Single and Double Potential Step

770   Chronoamperometry at a Disk Ultramicroelectrode. *Anal. Chem.* **69**, 2063–2069.

771   Mariotti A., Germon J. C., Hubert P., Kaiser P., Letolle R., Tardieux A. and Tardieux P. (1981)

772   Experimental determination of nitrogen kinetic isotope fractionation: Some principles;

773   illustration for the denitrification and nitrification processes. *Plant Soil* **62**, 413–430.

774   McGinnis D. F., Kirillin G., Tang K. W., Flury S., Bodmer P., Engelhardt C., Casper P. and

775   Grossart H. P. (2015) Enhancing surface methane fluxes from an oligotrophic lake:

776   Exploring the microbubble hypothesis. *Environ. Sci. Technol.* **49**, 873–880.

777 Nguyen T. B., Topçuoğlu B. D., Holden J. F., LaRowe D. E. and Lang S. Q. (2020) Lower

778   hydrogen flux leads to larger carbon isotopic fractionation of methane and biomarkers

779   during hydrogenotrophic methanogenesis. *Geochim. Cosmochim. Acta* **271**, 212–226.

780 Okumura T., Kawagucci S., Saito Y., Matsui Y., Takai K. and Imachi H. (2016) Hydrogen and

781   carbon isotope systematics in hydrogenotrophic methanogenesis under H2-limited and H2-

782   enriched conditions: implications for the origin of methane and its isotopic diagnosis. *Prog.*

783   *Earth Planet. Sci.* **3**, 1–19.

784 Ono S., Rhim J. H., Gruen D. S., Taubner H., Kölling M. and Wegener G. (2021) Clumped

785   isotopologue fractionation by microbial cultures performing the anaerobic oxidation of

786   methane. *Geochim. Cosmochim. Acta* **293**, 70–85.

787 Ono S., Wang D. T., Gruen D. S., Sherwood Lollar B., Zahniser M. S., McManus B. J. and

788   Nelson D. D. (2014) Measurement of a doubly substituted methane isotopologue, 13CH3D,

789   by tunable infrared laser direct absorption spectroscopy. *Anal. Chem.* **86**, 6487–6494.

790 Park S. H., Park C., Lee J. Y. and Lee B. (2017) A Simple Parameterization for the Rising

791   Velocity of Bubbles in a Liquid Pool. *Nucl. Eng. Technol.* **49**, 692–699.

792 Pauss A., Andre G., Perrier M. and Guiot S. R. (1990) Liquid-to-Gas mass transfer in anaerobic

793   processes: Inevitable transfer limitations of methane and hydrogen in the biomethanation

794   process. *Appl. Environ. Microbiol.* **56**, 1636–1644.

795 Penning H., Plugge C. M., Galand P. E. and Conrad R. (2005) Variation of carbon isotope

796   fractionation in hydrogenotrophic methanogenic microbial cultures and environmental

797   samples at different energy status. *Glob. Chang. Biol.* **11**, 2103–2113.

798   Pihl T. D., Sharma S. and Reeve J. N. (1994) Growth phase-dependent transcription of the genes

799   that encode the two methyl coenzyme M reductase isoenzymes and N5-

800   methyltetrahydromethanopterin:Coenzyme M methyltransferase in Methanobacterium

801   thermoautotrophicum ΔH. *J. Bacteriol.* **176**, 6384–6391.

802   Pohlman J. W., Kaneko M., Heuer V. B., Coffin R. B. and Whiticar M. (2009) Methane sources

803   and production in the northern Cascadia margin gas hydrate system. *Earth Planet. Sci. Lett.*

804   **287**, 504–512.

805   Rees C. E. (1973) A steady-state model for sulphur isotope fractionation in bacterial reduction

806   processes. *Geochim. Cosmochim. Acta* **37**, 1141–1162.

807   Reeve J. N., Nölling J., Morgan R. M. and Smith D. R. (1997) Methanogenesis: Genes,

808   Genomes, and Who's on First? *J. Bacteriol.* **179**, 5975–5986.

809   Robinson J. A. and Tiedje J. M. (1982) Kinetics of hydrogen consumption by rumen fluid,

810   anaerobic digestor sludge, and sediment. *Appl. Environ. Microbiol.* **44**, 1374–1384.

811   Rospert S., Linder D., Ellermann J. and Thauer R. K. (1990) Two genetically distinct methyl-

812   coenzyme M reductases in Methanobacterium thermoautotrophicum strain Marburg and

813   ΔH. *Eur. J. Biochem.* **194**, 871–877.

814   Scheller S., Goenrich M., Thauer R. K. and Jaun B. (2013) Methyl-Coenzyme M Reductase from

815   Methanogenic Archaea: Isotope E ff ects on the Formation and Anaerobic Oxidation of

816   Methane.

817   Schoell M. (1988) Multiple origins of methane in the Earth. *Chem. Geol.* **71**, 1–10.

818   Sherwood Lollar B., Lacrampe-Couloume G., Voglesonger K., Onstott T. C., Pratt L. M. and

819   Slater G. F. (2008) Isotopic signatures of CH4 and higher hydrocarbon gases from

820   Precambrian Shield sites: A model for abiogenic polymerization of hydrocarbons. *Geochim.*

821   *Cosmochim. Acta* **72**, 4778–4795.

822   Sherwood Lollar B., Westgate T. D., Ward J. A., Slater G. F. and Lacrampe-Couloume G. (2002)

823   Abiogenic formation of alkanes in the earth's crust as a minor source for global

824   hydrocarbon reservoirs. *Nature* **416**, 522–524.

825   Smolenski W. J. and Robinson J. A. (1988) In situ rumen hydrogen concentrations in steers fed

826   eight times daily, measured using a mercury reduction detector. *FEMS Microbiol. Lett.* **53**,

827   95–100.

828   Stewart L. C., Llewellyn J. G., Butterfield D. A., Lilley M. D. and Holden J. F. (2016) Hydrogen

829   and thiosulfate limits for growth of a thermophilic, autotrophic Desulfurobacterium species

830   from a deep-sea hydrothermal vent. *Environ. Microbiol. Rep.* **8**, 196–200.

831   Stolper D. A., Martini A. M., Clog M., Douglas P. M., Shusta S. S., Valentine D. L., Sessions A.

832   L. and Eiler J. M. (2015) Distinguishing and understanding thermogenic and biogenic

833   sources of methane using multiply substituted isotopologues. *Geochim. Cosmochim. Acta*

834   **161**, 219–247.

835   Stolper D. A., Sessions A. L., Ferreira A. A., Santos Neto E. V., Schimmelmann A., Shusta S. S.,

836   Valentine D. L. and Eiler J. M. (2014) Combined 13C-D and D-D clumping in methane:

837   Methods and preliminary results. *Geochim. Cosmochim. Acta* **126**, 169–191. Available at:

838   http://dx.doi.org/10.1016/j.gca.2013.10.045.

839   Teramoto M., Fujita S., Kataoka M. and Hashimoto K. (1970) Effect of Bubble Size on the

840   Selectivity of Consecutive Gas-Liquid Reactions. In *Meeting of the Society of the Chemical*

841   *Engineers (Japan)* pp. 79–82.

842   Thauer R. K. (2011) Anaerobic oxidation of methane with sulfate: On the reversibility of the

843   reactions that are catalyzed by enzymes also involved in methanogenesis from CO2. *Curr.*

844   *Opin. Microbiol.* **14**, 292–299.

845   Thauer R. K., Kaster A. K., Seedorf H., Buckel W. and Hedderich R. (2008) Methanogenic

846   archaea: Ecologically relevant differences in energy conservation. *Nat. Rev. Microbiol.* **6**,

847   579–591.

848   Topçuoğlu B. D., Meydan C., Orellana R. and Holden J. F. (2018) Formate hydrogenlyase and

849   formate secretion ameliorate H 2 inhibition in the hyperthermophilic archaeon

850   Thermococcus paralvinellae. *Environ. Microbiol.* **20**, 949–957.

851   Topçuoğlu B., Meydan C., Nguyen T., Lang S. and Holden J. F. (2019) Growth Kinetics, Carbon

852   Isotope Fractionation, and Gene Expression in the Hyperthermophile Methanocaldococcus

853   jannaschii during Hydrogen-Limited Growth and Interspecies Hydrogen Transfer Begüm.

854   **85**, 1–14.

855   Valentine D. L., Chidthaisong A., Rice A., Reeburgh W. S. and Tyler S. C. (2004) Carbon and

856   hydrogen isotope fractionation by moderately thermophilic methanogens. *Geochim.*

857   *Cosmochim. Acta* **68**, 1571–1590.

858   Wang D. T., Gruen D. S., Lollar B. S., Hinrichs K.-U., Stewart L. C., Holden J. F., Hristov A.

859   N., Pohlman J. W., Morrill P. L., Könneke M., Delwiche K. B., Reeves E. P., Sutcliffe C.

860   N., Ritter D. J., Seewald J. S., McIntosh J. C., Hemond H. F., Kubo M. D., Cardace D.,

861   Hoehler T. M. and Ono S. (2015) Nonequilibrium clumped isotope signals in microbial

862   methane. *Science (80-.).* **348**, 428–431.

863   Welhan J. A. and Lupton J. E. (1987) Light hydrocarbon gases in Guaymas Basin hydrothermal

864   fluids: thermogenic versus abiogenic origin. *Am. Assoc. Pet. Geol. Bull.* **71**, 215–223.

865   Whiticar M. J. (1990) A geochemial perspective of natural gas and atmospheric methane. *Org.*

866   *Geochem.* **16**, 531–547.

867 Whiticar M. J. (1999) Carbon and hydrogen isotope systematics of bacterial formation and

868   oxidation of methane. *Chem. Geol.* **161**, 291–314.

869 Wolfe R. S. (2011) *Techniques for cultivating methanogens.* 1st ed., Elsevier Inc.

870 Yoshioka H., Sakata S. and Kamagata Y. (2008) Hydrogen isotope fractionation by

871   Methanothermobacter thermoautotrophicus in coculture and pure culture conditions.

872   *Geochim. Cosmochim. Acta* **72**, 2687–2694.

873 Young E. D., Kohl I. E., Lollar B. S., Etiope G., Rumble D., Li (李姝宁) S., Haghnegahdar M.

874   A., Schauble E. A., McCain K. A., Foustoukos D. I., Sutclife C., Warr O., Ballentine C. J.,

875   Onstott T. C., Hosgormez H., Neubeck A., Marques J. M., Pérez-Rodríguez I., Rowe A. R.,

876   LaRowe D. E., Magnabosco C., Yeung L. Y., Ash J. L. and Bryndzia L. T. (2017) The

877   relative abundances of resolved l2CH2D2 and 13CH3D and mechanisms controlling

878   isotopic bond ordering in abiotic and biotic methane gases. *Geochim. Cosmochim. Acta* **203**,

879   235–264.

880 Young E. D., Rumble D., Freedman P. and Mills M. (2016) A large-radius high-mass-resolution

881   multiple-collector isotope ratio mass spectrometer for analysis of rare isotopologues of O2,

882   N2, CH4 and other gases. *Int. J. Mass Spectrom.* **401**, 1–10.

883

884

Tables

Table 1. Summary of experiments.

Experiment	Organism	Temp. (°C)	$x\mathrm{H_2}$ (%)	System
B.82	*Methanocaldococcus bathoardescens*	82	80	Batch
F.82.80	*Methanocaldococcus bathoardescens*	82	80	Fed-batch
F.82.25	*Methanocaldococcus bathoardescens*	82	25	Fed-batch
F.60.80	*Methanocaldococcus bathoardescens*	60	80	Fed-batch
F65.20	*Methanothermobacter thermautotrophicus* (ΔH)	65	20	Fed-batch
F.65.5	*Methanothermobacter thermautotrophicus* (ΔH)	65	5→1.6	Fed-batch

Table 2. Parameters used for model calculation described in 2.3.7.

Parameter	Values used (range)	Sources/Notes
r_b	0.05 cm (0.025 to 0.1 cm)	Teramoto *et al.* (1970)
D	5×10^{-5} cm^2/sec	Macpherson and Unwin (1997)
A_b	200 cm^2	Calculated for a gas flow rate of 200 mL/min, medium height of 20 cm, and bubble radius of 0.05 cm; Park et al. (2017)
A_h	177 cm^2	Calculated for a known reactor I.D. = 15 cm

Table 3. Results for batch culture experiment (Experiment B.82). *Methanocaldococcus bathoardescens* was grown at 82 °C on 80% H_2. The headspace pressure decreased, as 5 moles of gas were consumed to produce 1 mole of gas (Eqn. 7). Therefore, volumes (in mL) of H_2, CO_2, and CH_4 were calculated assuming 4:1:1 reaction stoichiometries and mixing ratios for H_2: CO_2:CH_4 measure by GC (Table 3; Supplementary Material, Figure S1).

Time (h)	cells/mL	H_2 (mL)[†]	CO_2 (mL)[†]	CH_4 (mL)[†]	$\delta^{13}C_{CO2}$ (‰)	$\delta^{13}C_{CH4}$ (‰)	δD_{H2O} (‰)	δD_{CH4} (‰)	$\Delta^{13}CH_3D$ (‰)	CI
0.0	-	288.24	47.35	0.13	-34.9	-	-45.4	-	-	-
1.0	1.1E+6	281.61	50.49	0.53	-	-	-46.9	-	-	-
1.9	5.5E+6	258.65	44.57	6.83	-31.4	-	-	-	-	-
3.0	3.7E+7	125.88	13.33	36.98	-14.3	-47.1	-46.5	-407.6	0.48	0.20
4.0	3.6E+7	78.29	4.55	48.45	-25.1	-39.5	-	-409.6	0.38	0.19
5.0	7.4E+7	68.78	2.84	50.48	-	-	-	-	-	-
6.0	7.1E+7	35.52	2.60	58.35	-22.0	-	-	-	-	-
6.9	4.3E+7	53.28	2.11	53.90	-	-38.8	-46.0	-413.3	0.32	0.26

[†] volume of gas calculated based on mixing ratios and expected headspace pressure at the time of measurement; – values not determined; CI is the 95% confidence interval in permil (‰).

897 Table 4. Results for fed-batch experiments. *Methanocaldococcus bathoardescens* was grown at 82 °C and 80% H_2 (F.82.80); at 60 °C and 80% H_2 (F.60.80); and
898 at 82 °C and 25% H_2 (F.82.25).

Experiment	Temp (°C)	Time (h)	cells/mL	H_2 (%)	CO_2 (%)	CH_4 (%)	MPR (mol/h)	csMPR (pmol/cell/h)	$\delta^{13}C_{CO2}$ (‰)	$\delta^{13}C_{CH4}$ (‰)	$\alpha_{CH4\ CO2}$	δD_{H2O} (‰)	δD_{CH4} (‰)	$\alpha_{CH4\ H2O}$	$\Delta^{13}CH_3D$ (‰)	CI
F.82.80	82	0.0	6.8E+5	79.8	19.9	0.08	4.1E-04	0.33	-39.9	-	*	-53.7	-	*	-	-
F.82.80	82	0.0	-	80.7	19.5	1.78	8.0E-03	-	-	-	*	-	-	*	-	-
F.82.80	82	1.1	5.2E+6	-	-	-	-	-	-	-	*	-	-	*	-	-
F.82.80	82	1.5	-	76.6	20.0	3.75	1.6E-02	-	-25.8	-68.2	0.957	-53.8	-362.6	0.674	1.25	0.48
F.82.80	82	2.2	2.0E+7	77.2	19.8	4.03	1.7E-02	0.47	-21.3	-76.6	0.944	-	-336.9	*	0.38	0.43
F.82.80	82	2.5	2.8E+7	77.9	18.5	4.02	1.7E-02	0.34	-	-74.3	*	-	-331.8	*	-0.17	0.49
F.82.80	82	3.0	3.2E+7	78.0	18.6	4.09	1.7E-02	0.29	-	-80.2	*	-	-333.6	*	0.07	0.83
F.82.80	82	3.5	4.1E+7	-	-	-	-	-	-	-	*	-	-	*	-	-
F.82.80	82	3.7	4.5E+7	77.0	19.2	3.92	1.7E-02	0.21	-	-77.9	*	-	-331.8	*	-0.29	0.47
F.60.80	60	0.0	5.8E+6	75.5	21.9	0.06	3.1E-04	0.03	-	-	*	-	-	*	-	-
F.60.80	60	1.5	1.7E+7	73.9	22.3	0.47	2.4E-03	0.08	-38.8	-56.4	0.982	-	-305.0	*	2.06	-
F.60.80	60	1.8		75.3	22.1	0.50	2.6E-03	-	-	-	*	-	-	*	-	-
F.60.80	60	2.8	1.4E+7	73.1	22.4	1.38	6.9E-03	0.28	-	-	*	-	-	*	-	-
F.60.80	60	3.3		75.1	22.2	1.90	9.0E-03	-	-36.8	-60.1	0.976	-	-364.5	*	1.52	0.58
F.60.80	60	3.8	2.4E+7	72.5	21.1	2.98	1.4E-02	0.32	-	-	*	-	-	*	-	-
F.60.80	60	5.6	1.3E+8	74.0	21.1	4.14	1.8E-02	0.08	-	-	*	-	-	*	-	-
F.60.80	60	6.4		74.5	21.0	3.94	1.7E-02	-	-33.6	-68.9	0.964	-	-321.4	*	0.80	0.28
F.60.80	60	6.7	1.1E+8	71.7	21.3	3.64	1.7E-02	0.08	-	-	*	-	-	*	-	-
F.60.80	60	7.8	1.4E+8	73.9	21.4	3.91	1.7E-02	0.07	-	-	*	-	-	*	-	-
F.60.80	60	8.9	1.9E+8	71.7	21.2	3.7	1.7E-02	0.05	-	-	*	-	-	*	-	-
F.60.80	60	9.4		73.7	21.6	4.07	1.8E-02	-	-32.6	-67.5	0.964	-	-314.6	*	0.06	0.17
F.82.25	82	0.0	1.0E+6	23.1	21.8	BDL	-	-	-	-	*	-	-	*	-	-
F.82.25	82	0.2		23.1	21.9	0.03	1.6E-04	-	-14.0	-50.8	0.963	-40.4	-358.8	0.668	1.15	0.42
F.82.25	82	0.5	4.4E+6	22.8	23.6	0.41	2.1E-03	0.27	-	-	*	-	-	*	-	-
F.82.25	82	1.7	1.3E+7	22.6	22.9	1.30	5.8E-03	0.25	-	-	*	-39.9	-	*	-	-
F.82.25	82	2.3	9.1E+6	22.5	23.8	1.39	6.1E-03	0.37	-	-	*	-	-	*	-	-
F.82.25	82	2.8	9.6E+6	22.4	23.5	1.53	6.6E-03	0.38	-	-	*	-40.1	-	*	-	-
F.82.25	82	3.6	2.1E+7	22.4	23.8	1.56	6.7E-03	0.18	-	-	*	-	-	*	-	-
F.82.25	82	4.4	7.4E+6	22.5	23.9	1.47	6.4E-03	0.48	-	-	*	-40.0	-	*	-	-
F.82.25	82	4.9	2.4E+7	22.4	24.2	1.57	6.7E-03	0.16	-	-	*	-	-	*	-	-
F.82.25	82	5.2	2.8E+7	16.7	22.8	1.41	7.8E-03	0.15	-	-	*	-	-	*	-	-
F.82.25	82	19.0	2.0E+8	22.6	23.6	1.69	7.1E-03	0.02	-	-	*	-	-	*	-	-
F.82.25	82	22.5	1.0E+8	22.6	23.9	1.51	6.5E-03	0.04	-	-	*	-	-	*	-	-
F.82.25	82	24.5	9.6E+7	22.6	23.3	1.57	6.7E-03	0.04	-	-	*	-	-	*	-	-
F.82.25	82	24.7		22.4	23.9	1.82	7.5E-03	-	-12.0	-70.8	0.941	-	-328.6	*	-0.78	0.73
F.82.25	82	25.8	8.1E+7	22.5	23.0	1.65	7.0E-03	0.05	-	-	*	-	-	*	-	-
F.82.25	82	26.8	1.0E+8	22.2	2.0	2.05	8.3E-03	0.05	-	-	*	-	-	*	-	-
F.82.25	82	43.7	1.5E+8	21.6	23.8	2.82	1.1E-02	0.04	-	-	*	-	-	*	-	-
F.82.25	82	44.4		21.6	24.8	2.71	1.0E-02	-	-9.9	-67.8	0.941	-	-327.7	*	-0.65	0.36
F.82.25	82	45.2		21.7	23.3	2.89	1.1E-02	-	-10.3	-65.4	0.944	-38.6	-364.5	0.661	-0.42	0.53
F.82.25	82	52.5	2.1E+8	21.2	24.9	2.62	1.0E-02	0.03	-	-	*	-	-	*	-	-

899
900 – values not determined; * not applicable; CI is the 95% confidence interval in permil (‰).

901 Table 5. Results for fed-batch experiments. *Methanothermobacter thermautotrophicus* was grown at 65 °C and 20% H_2 (Experiment F.65.20) and at 65 °C and 5–
902 1.6% H_2 (Experiment F.65.5).

Experiment	Time (h)	cells/mL	H_2 (%)	CO_2 (%)	CH_4 (%)	MPR (mol/h)	csMPR (pmol/cell/h)	$\delta^{13}C_{CO2}$ (‰)	$\delta^{13}C_{DIC}$ (‰)	$\alpha_{CO2-DIC}$	$\delta^{13}C_{CH4}$ (‰)	$\alpha_{CH4-CO2}$	δD_{H2O} (‰)	δD_{CH4} (‰)	$\alpha_{CH4-H2O}$	$\Delta^{13}CH_3D$ (‰)	CI
F.65.20	0.0	2.3E+5	21.6	18.7	0.01	4.1E-05	0.098	-15.3	-11.7	0.996	-	*	-45.5	-	*	-	-
F.65.20	2.2	4.8E+5	21.2	19.4	0.03	1.4E-04	0.158	-	-	*	-	*	-	-	*	-	-
F.65.20	5.8	1.2E+6	21.1	19.3	0.10	4.5E-04	0.213	-	-	*	-	*	-	-	*	-	-
F.65.20	11.7	4.8E+6	19.9	19.3	0.44	2.0E-03	0.237	-14.9	-10.5	0.996	-48.4	0.966	-45.5	-361.8	0.669	0.33	0.57
F.65.20	22.8	4.8E+7	19.5	17.9	0.69	3.0E-03	0.035	-14.9	-9.7	0.995	-57.0	0.957	-	-363.3	0.667	-2.03	0.50
F.65.20	25.7	6.9E+7	19.5	18.1	0.70	3.1E-03	0.025	-	-	*	-	*	-	-	*	-	-
F.65.20	28.1	7.7E+7	19.5	18.1	0.70	3.1E-03	0.022	-	-9.7	*	-	*	-45.5	-	*	-	-
F.65.20	33.3	1.1E+8	19.5	18.1	0.71	3.1E-03	0.016	-14.0	-	*	-	*	-	-	*	-	-
F.65.20	47.2	1.8E+8	19.3	18.7	0.72	3.2E-03	0.010	-13.9	-9.4	0.995	-62.1	0.951	-	-347.0	0.684	-1.28	0.87
F.65.20	53.2	2.1E+8	19.2	19.3	0.74	3.3E-03	0.009	-13.6	-9.5	0.996	-	*	-	-	*	-	-
F.65.20	70.2	2.9E+8	19.3	18.1	0.76	3.3E-03	0.007	-	-	*	-	*	-	-	*	-	-
F.65.20	77.0	2.7E+8	19.3	19.0	0.76	3.3E-03	0.007	-13.6	-9.4	0.996	-62.9	0.950	-	-352.3	0.679	-1.09	0.65
F.65.20	94.9	3.1E+8	19.4	18.8	0.78	3.4E-03	0.006	-	-	*	-	*	-	-	*	-	-
F.65.20	101.9	4.5E+8	19.0	18.9	0.81	3.6E-03	0.004	-13.8	-9.6	0.996	-63.3	0.950	-	-351.4	0.677	-1.91	0.54
F.65.20	102.4	3.9E+8	19.2	19.5	0.80	3.5E-03	0.005	-	-	*	-	*	-	-	*	-	-
F.65.20	119.2	4.1E+8	18.9	19.5	0.80	3.5E-03	0.005	-	-	*	-	*	-41.4	-	*	-	-
F.65.5	0.0	2.8E+5	4.9	20.3	0.01	5.2E-05	0.103	-15.7	-11.4	0.996	-	-	-44.9	-	*	-	-
F.65.5	1.7	4.7E+5	4.8	19.6	0.04	1.8E-04	0.210	-	-	*	-	-	-	-	*	-	-
F.65.5	4.9	1.1E+6	4.5	20.7	0.09	4.7E-04	0.252	-	-	*	-	-	-	-	*	-	-
F.65.5	9.4	2.5E+6	4.4	19.7	0.1	7.0E-04	0.156	-	-	*	-58.0	0.957	-	-364.1	0.666	1.28	0.98
F.65.5	10.5		-	-	-	-	-	-15.5	-11.4	0.996	-	-	-	-	*	-	-
F.65.5	11.8	5.9E+6	4.4	19.6	0.14	7.1E-04	0.068	-	-	*	-	-	-	-	*	-	-
F.65.5	21.9	1.4E+7	4.3	20.5	0.16	7.9E-04	0.031	-	-	*	-67.0	0.947	-	-371.7	0.658	-2.06	0.47
F.65.5	23.3		-	-	-	-	-	-15.2	-10.9	0.996	-	-	-45.5	-	*	-	-
F.65.5	27.5	2.5E+7	4.4	19.3	0.16	7.7E-04	0.017	-	-	*	-	-	-	-	*	-	-
F.65.5	30.3	2.7E+7	4.4	19.0	0.16	7.7E-04	0.016	-	-11.0	*	-	-	-	-	*	-	-
F.65.5	46.0	5.1E+7	4.3	20.6	0.17	8.2E-04	0.009	-	-	*	-	-	-	-	*	-	-
F.65.5	54.0	5.8E+7	4.3	19.5	0.17	8.5E-04	0.008	-15.3	-11.3	0.996	-70.6	0.944	-45.2	-368.4	0.661	-2.92	0.84
F.65.5	72.5	6.6E+7	1.6	20.3	0.06	2.5E-04	0.002	-15.6	-11.5	0.996	-77.5	0.937	-	-365.3	0.665	-2.52	0.46
F.65.5	95.3	7.2E+7	1.6	20.1	0.06	2.5E-04	0.002	-	-	*	-76.9	0.938	-	-370.0	0.660	-4.13	0.46
F.65.5	97.3		-	-	-	-	-	-15.6	-11.4	0.996	-	-	-	-	*	-	-
F.65.5	119.4	7.0E+7	1.5	21.4	0.06	2.6E-04	0.002	-	-	*	-	-	-	-	*	-	-

903

904 – values not determined; * not applicable; CI is the 95% confidence interval in permil (‰)

Figure Captions

906 **Figure 1.** Schematic diagram of the fed-batch culturing system

907 **Figure 2.** Schematic overview of the biochemical pathway involved in hydrogenotrophic

908 methanogenesis and isotopologue flow network model scenarios in this study. (A) Overview of

909 the biochemical pathway and enzymes associated with each step. Grey bubbles represent pools of

910 cellular carbon, grouped into those with the same redox state. The four H-addition steps are labeled

911 with numbers. Fd_{red}, reduced ferredoxin; Fd_{ox}, oxidized ferredoxin; MFR, methanofuran; H_4MPT,

912 tetrahydromethanopterin; F_{420}, coenzyme F_{420}; CoM-HS, coenzyme M; CoB-SH, coenzyme B; Ftr,

913 formyl-MFR: H_4MPT formyltransferase; Mch, N^5,N^{10}-methenyl- H_4MPT cyclohydrolase; Mtd,

914 F_{420}-dependent N^5,N^{10}-methylene-H_4MPT dehydrogenase; Hmd, H_2-forming N^5,N^{10}-methylene-

915 H_4MPT dehydrogenase; Mer, F_{420}-dependent N^5,N^{10}-methylene-H_4MPT reductase; Mtr, N^5-

916 methyl- H_4MPT:CoM methyltransferase; Mcr, methyl CoM reductase. Panels B, C and D show

917 the three model scenarios tested in this study. K_m values are effective half-saturation constants

918 used to assign reversibilities to H-addition steps. (B) Equilibrium end-member scenario has a K_m

919 value of 10^4 M for all four H-addition steps. (C) Uniform reversibility scenario has a K_m value of

920 10^{-8} M for all four H-addition steps. (D) In differential reversibility scenario, the last step is less

921 reversible compared to the preceding three H-addition steps ($K_m = 5 \times 10^{-5}$ M for the first three

922 steps; $K_m = 10^{-8}$ M for the last step).

923 **Figure 3.** Summary of fed-batch experiment results of this study. Each column (columns A–E)

924 shows the result for each fed-batch experiment. The experiment names and conditions can be found

925 at the top of each column. Each row (rows 1–6) shows a type of data. Modeled values of dissolved

926 hydrogen concentration or [H_2] (μM; row 1), cell density (cells/mL; row 2), methane production

927 rate or MPR (μmol/sec; row 3), carbon isotope fractionation factor or $^{13}\alpha$ (row 4), hydrogen isotope

928   fractionation factor or $^2\alpha$ (row 5), and methane clumped isotope abundance or $\Delta^{13}CH_3D$ (‰; row

929   6). For the [H_2] model results (row 1), open squares represent maximum [H_2] values expected at

930   equilibrium with the dry headspace mixing ratios (xH_2). Filled circles represent [H_2] values

931   expected at equilibrium that are corrected for saturation water vapor pressure (pH_2O_{sat}) at

932   respective temperatures (0.51 bars at 82 °C, 0.25 bars at 65 °C and 0.20 bars at 60 °C). Triangles

933   represent pH_2O_{sat}-corrected [H_2] values expected during methane production with two different

934   k_La values: 700 h^{-1} (down-pointing yellow triangles) and 350 h^{-1} (up-pointing blue triangles).

935   Refer to 2.3.7 for details. Grey horizontal lines in rows 4–6 represent the equilibrium $^{13}\alpha$, $^2\alpha$ and

936     $\Delta^{13}CH_3D$ values expected at respective experimental temperatures. Grey vertical lines in column

937   5 for F.65.5 indicate the time at which xH_2 was switched from 5% to 1.6%. Each panel shares the

938   y-axis with the panel to its left unless new axis tick marks are introduced. Note that the durations

939   of experiments vary across experiments.

940   **Figure 4.** Changes in carbon ($^{13}\alpha$) and hydrogen ($^2\alpha$) isotope fractionation factors and $\Delta^{13}CH_3D$

941   values during hydrogenotrophic methanogenesis. Panels A, B and C, respectively, show $^{13}\alpha$, $^2\alpha$

942   and $\Delta^{13}CH_3D$ values measured in this study and reported in the literature, as a function of H_2 partial

943   pressure (pH_2) in the supply gas. Color triangle and diamond symbols represent data from this

944   study. Grey circles in panels A and B represent the $^{13}\alpha$ and $^2\alpha$ values from the literature (Games

945   and Hayes, 1978; Fuchs *et al.*, 1979; Belyaev *et al.*, 1983; Balabane *et al.*, 1987; Krzycki *et al.*,

946   1987; Botz *et al.*, 1996; Valentine *et al.*, 2004; Yoshioka, Sakata and Kamagata, 2008; Hattori *et*

947   *al.*, 2012; Kawagucci *et al.*, 2014). Grey symbols in panel C represent the $\Delta^{13}CH_3D$ values obtained

948   from pure culture hydrogenotrophic methanogenesis experiments in closed systems (Gruen *et al.*,

949   2018 and references therein). Filled and open circles represent thermophilic and mesophilic

950   temperatures, respectively. Dashed lines represent the $^{13}\alpha$, $^2\alpha$ and $\Delta^{13}CH_3D$ values expected at
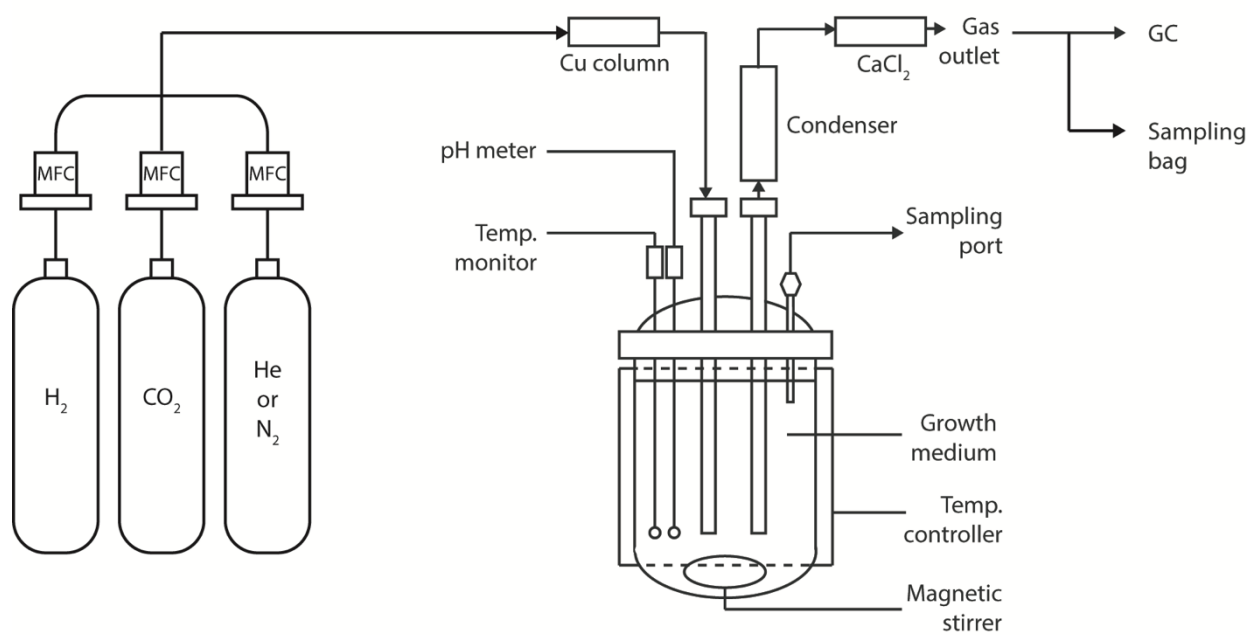
951   equilibrium at temperatures indicated in the legend.

952   **Figure 5.** Modeled carbon ($\delta^{13}C$) and hydrogen (δD) isotope and clumped isotopologue

953   compositions ($\Delta^{13}CH_3D$) of methane produced via hydrogenotrophic methanogenesis. Panel A, B,

954   and C show the modeled $\delta^{13}C$, δD and $\Delta^{13}CH_3D$ values of methane, respectively. Dotted lines

955   (yellow) show the model results at 82 °C for the equilibrium end-member scenario ($K_m = 10^4$ M

956   for all φ values). Dashed lines (red) show the results for the uniform reversibility scenario ($K_m =$

957   10^{-8} M for all φ values). Solid lines (blue) show a differential reversibility scenario, where the last

958   H-addition step is less reversible compared to the preceding three H-addition steps ($K_m = 5 \times 10^{-5}$

959   M for φ_{1-3}, $K_m = 10^{-8}$ M for φ_4).

960   **Figure 6.** Carbon ($^{13}\alpha$) and hydrogen ($^2\alpha$) isotope fractionation factors and $\Delta^{13}CH_3D$ values as a

961   function of modeled dissolved H_2 concentration, $[H_2]$. Panel A shows the typical ranges of $[H_2]$

962   observed in natural environments and culture studies. The $[H_2]$ ranges for batch cultures studies

963   were calculated assuming 1–2 bars of 80% H_2 in the headspace at 25 °C. Note that the pH_2 values

964   for batch co-cultures (Okumura et al., 2016) are based on headspace mixing ratios and that $[H_2]$ in

965   the co-cultures are likely higher than $[H_2]^{eq}$ expected in equilibrium with pH_2. Panels B, C and D

966   compare the result of the isotopologue flow network model and experimental data from this study.

967   Color symbols and corresponding experiment names are shown in the legend. Horizontal dashed

968   lines represent the $^{13}\alpha$, $^2\alpha$ and $\Delta^{13}CH_3D$ values expected at equilibrium at corresponding

969   temperatures as shown in the legend. Solid lines are modeled trajectories of $^{13}\alpha$, $^2\alpha$ and $\Delta^{13}CH_3D$

970   for the differential reversibility scenario based on the isotopologue flow network model results

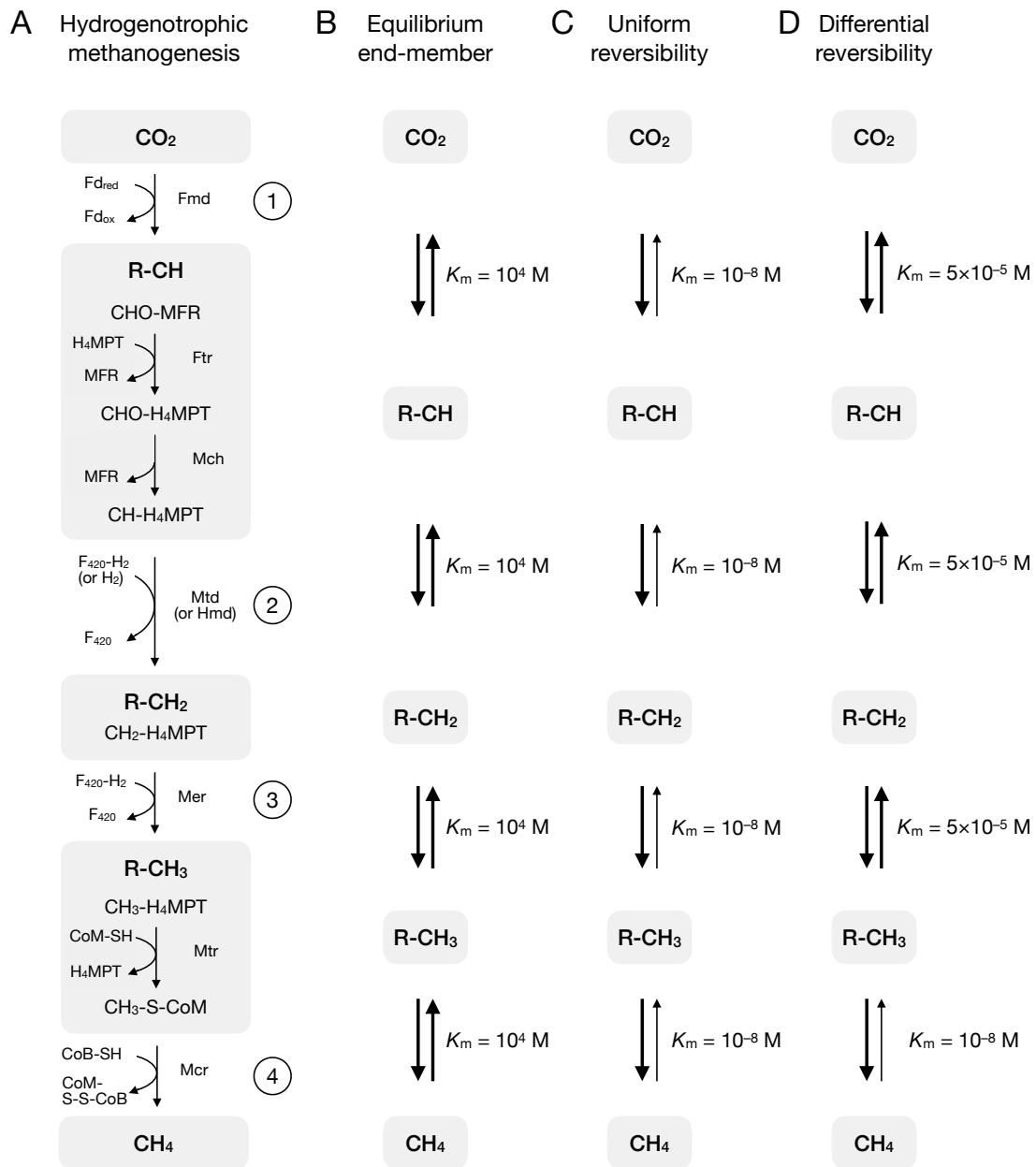971   (see Figure 5).

972

973 **Figures**
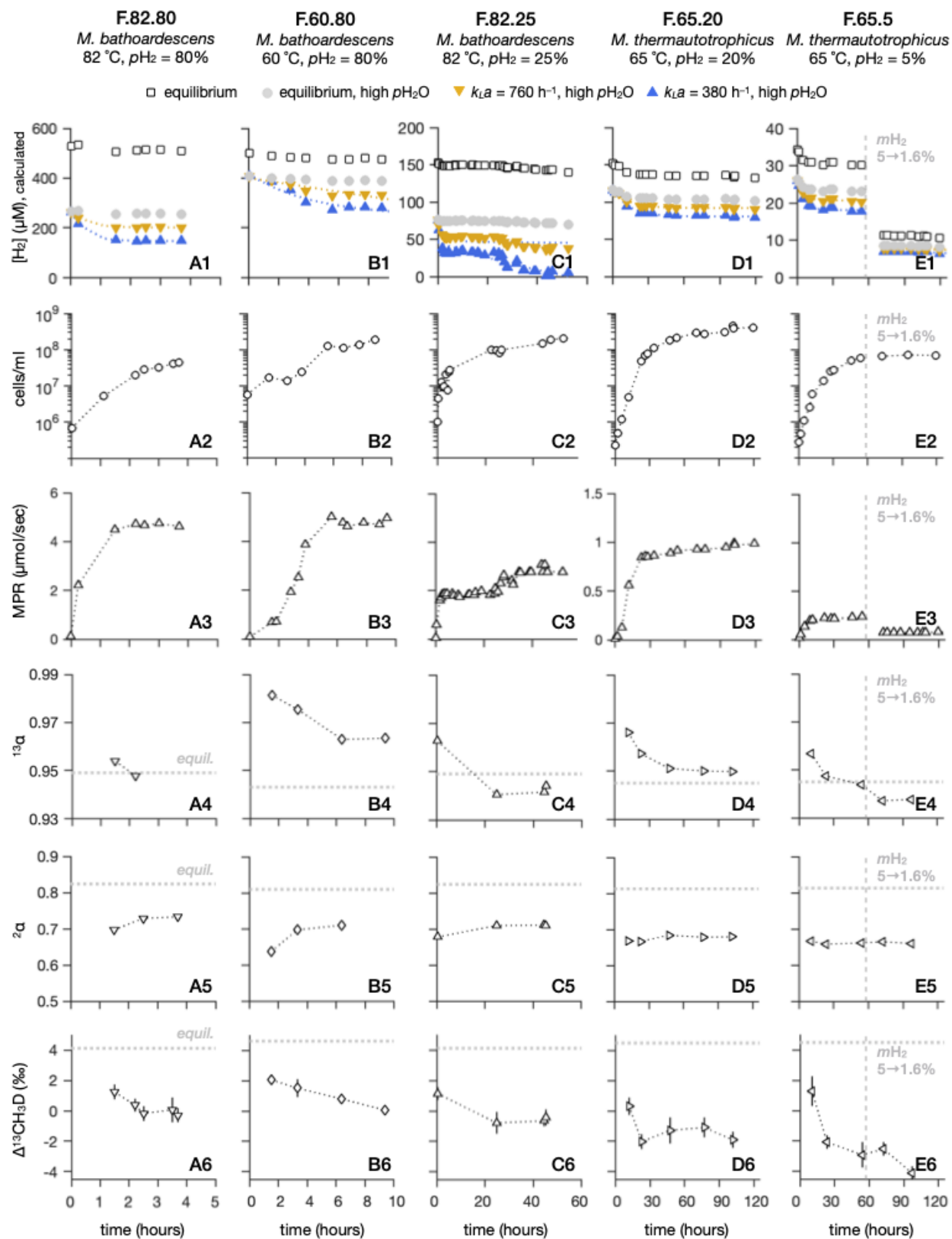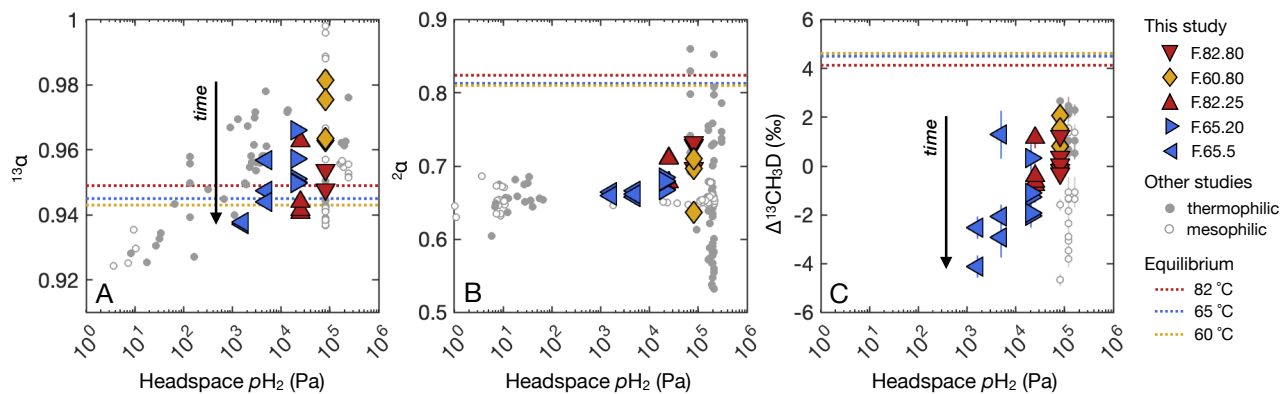
974

975

976 **Figure 1**

A Hydrogenotrophic methanogenesis

B Equilibrium end-member

C Uniform reversibility

D Differential reversibility

Column A — Hydrogenotrophic methanogenesis

CO_2

Fd_{red}, Fd_{ox}, Fmd — (1)

R-CH
CHO-MFR
H_4MPT, MFR, Ftr
CHO-H_4MPT
MFR, Mch
CH-H_4MPT

F_{420}-H_2 (or H_2), Mtd (or Hmd), F_{420} — (2)

R-CH$_2$
CH_2-H_4MPT

F_{420}-H_2, F_{420}, Mer — (3)

R-CH$_3$
CH_3-H_4MPT
CoM-SH, H_4MPT, Mtr
CH_3-S-CoM

CoB-SH, CoM-S-S-CoB, Mcr — (4)

CH_4

Column B — Equilibrium end-member

CO_2
$K_m = 10^4$ M
R-CH
$K_m = 10^4$ M
R-CH$_2$
$K_m = 10^4$ M
R-CH$_3$
$K_m = 10^4$ M
CH_4

Column C — Uniform reversibility

CO_2
$K_m = 10^{-8}$ M
R-CH
$K_m = 10^{-8}$ M
R-CH$_2$
$K_m = 10^{-8}$ M
R-CH$_3$
$K_m = 10^{-8}$ M
CH_4

Column D — Differential reversibility

CO_2
$K_m = 5\times10^{-5}$ M
R-CH
$K_m = 5\times10^{-5}$ M
R-CH$_2$
$K_m = 5\times10^{-5}$ M
R-CH$_3$
$K_m = 10^{-8}$ M
CH_4

977
978 **Figure 2**

48

F.82.80
M. bathoardescens
82 ℃, pH₂ = 80%

F.60.80
M. bathoardescens
60 ℃, pH₂ = 80%

F.82.25
M. bathoardescens
82 ℃, pH₂ = 25%

F.65.20
M. thermautotrophicus
65 ℃, pH₂ = 20%

F.65.5
M. thermautotrophicus
65 ℃, pH₂ = 5%

□ equilibrium ● equilibrium, high pH_2O ▼ $k_La = 760$ h⁻¹, high pH_2O ▲ $k_La = 380$ h⁻¹, high pH_2O

979
980
981 **Figure 3**

49

982
983 **Figure 4**

984

985

986
987
988 **Figure 5**

989

990   **Figure 6**